Frustration Driven Lattice Distortion in $Y_2Mo_2O_7$

Research Thesis

Submitted in Partial Fulfillment of the Requirements for the Degree of Master of Science in Physics

Eva Sagi

SUBMITTED TO THE SENATE OF THE TECHNION -
ISRAEL INSTITUTE OF TECHNOLOGY
ELUL 5764 HAIFA SEPTEMBER 2004

The research thesis was done under the supervision of Prof. Amit Keren in the department of physics.

THE GENEROUS FINANCIAL HELP OF THE TECHNION IS GRATEFULLY ACKNOWLEDGED.

Contents

List of Tables

List of Figures

Abstract

A frustrated system is one whose symmetry precludes the possibility that every pairwise interaction in the system can be satisfied at the same time. Such systems can have a disordered ground state with "macroscopic" degeneracy; that is, one that comprises a huge number of equivalent states of the same energy. Such a degeneracy prevents the system from settling into a single ground state as temperature is lowered. In real materials the ground state is selected by perturbations to the Hamiltonian whose ground state is degenerate. In this work we investigate the possibility of removing the frustration of the Heisenberg AF Hamiltonian on the pyrochlore lattice, a lattice of corner sharing tetrahedra, via a magnetoelastic coupling of the spins to the lattice, which enables the lattice to distort, thus relieving the degeneracy. We chose $Y_2Mo_2O_7$ as a candidate to look for frustration-driven distortion, since the spin-glass transition this compound undergoes hints at some kind of disorder in the exchange integral, whose origin is unknown. This disorder might be caused by a lattice distortion, for which there exist previous experimental evidence. We studied the compound using μSR and DC magnetization, and since we obtained inconclusive magnetic evidence for a lattice distortion, we were motivated to further investigate the nature of a magnetoelastic distortion in the pyrochlore lattice using computer simulations. We modelled the pyrochlore lattice in the presence of a distortion inducing term in the Hamiltonian, and sought its minimum energy state at T=0. Then we looked into the transformation this state undergoes as temperature is increased, in order to find the similarities between the idealized computer simulation and our real-life compound. We discovered that the magnetic characteristics of the ground state persist above the temperature at which the spatial signature of the distortion disappears, and this might explain why we see only magnetic evidence for a lattice distortion.

List of symbols and abbreviations

Symbol	Meaning
Y	Yttrium
Mo	Molybdenum
O	Oxigen
$\mathbf{S}$	Electronic spin
J	The exchange integral
H_0	The Heisenberg Hamiltonian
$H_{magnetoelastic}$	The magnetoelastic term in the Hamiltonian
$H_{elastic}$	The elastic term in the Hamiltonian
E	Energy
J'	Location derivative of the exchange integral
A_1	The singlet vibrational mode for a tetrahedron
E	The doublet vibrational mode for a tetrahedron
T_2	The triplet vibrational mode for a tetrahedron
q_A	The singlet normal coordinate for a tetrahedron
q_1,q_2	The doublet normal coordinates for a tetrahedron
q_A	The bilinear combination of the spin operators in the singlet represenation
f_1,f_2	The bilinear combinations of the spin operators in the doublet representation
$q = 0$	A distortion of the pyrochlore lattice induced by a zero wavevector phonon
K	Kelvin
μ_B	Bohr magneton
SG	Spin-glass
T_g	Temperature of spin-glass transition
μSR	Muon-spin rotation/relaxation/resonance

Symbol	Meaning
DC	Direct current
AC	Alternating current
A^0	Angstrom
NMR	Nuclear magnetic resonance
γ_μ	Muon gyromagnetic ratio
m_μ	Muon mass
ϵ	Energy of positron emitted in muon decay
a	asymmetry parameter
LF	Longitudinal field
TF	Transverse field
ZF	Zero Field
GPS	General purpose surface muons
PSI	Paul Scherrer Institut
CW	Continuous wave
F,B,U,D,R	Forward, Backward, Up, Down, Right positron detectors
$P(t)$	Muon polarization
$A_r(t)$	Raw experimental asymmetry
$A(t)$	Corrected asymmetry
α	Alpha parameter in μSR
Bg	Positron background
R_{TF}	Relaxation rate in a TF experiment
R_{LF}	Relaxation rate in a LF experiment
RRF	Rotating reference frame
Δ	Muon relaxation under the influence of static field distribution
χ	Magnetic susceptibility
$\mathbf{I}$	Muon spin

Chapter 1

Introduction

The concept of geometric frustration dates back to 1950, when the special properties of spins with antiferromagnetic exchange interaction on a triangular lattice were first discovered. Magnetic geometric frustration arises when the arrangement of spins on a lattice does not enable satisfying all near-neighbor spin-spin interactions at the same time. The simplest case is provided by three antiferromagnetically coupled spins in the corners of an equilateral triangle; if two spins are antiparallel to each other, the third spin can not be antiparallel to both of them. In order to satisfy two of the spin-spin interactions, the third one has to be frustrated (see Fig. (1.1)); this stems from the symmetrical geometric arrangement, hence the term "geometric frustration".

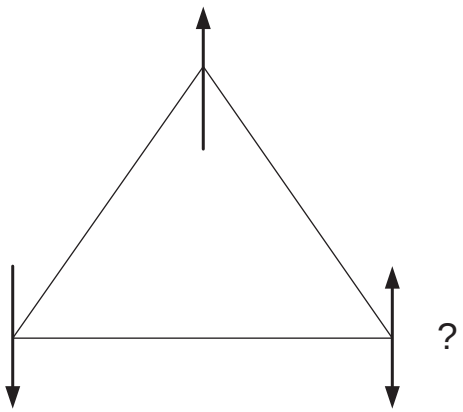

Figure 1.1: Three antiferromagnetically interacting spins in a triangular arrangement; one of the spins cannot be antiparallel to both its neighbours

Things get even more complicated for antiferromagnetic interactions between spins in the corners of a tetrahedron. In this case, two of the bonds

are frustrated, as shown in Fig. (1.2).

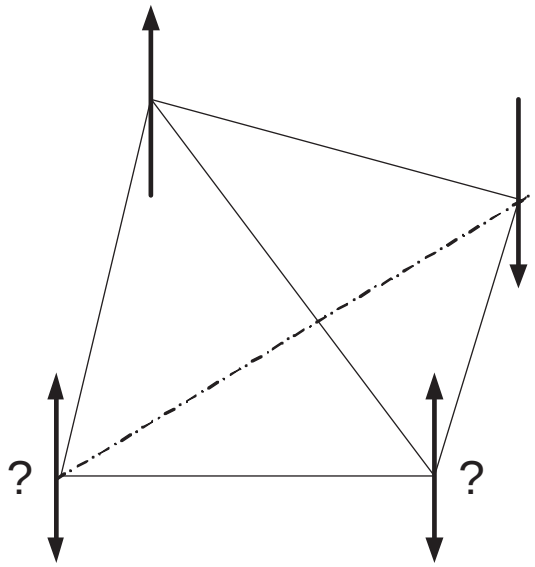

Figure 1.2: Four antiferromagnetically interacting spins in the corners of a tetrahedron; two of the interactions are frustrated.

Why is there interest in geometrically frustrated magnetic materials? It is precisely because the presence of frustration prevents the easy formation of spin-ordered states, and instead, exotic ground states are found such as spin glasses (where the spins freeze in a random pattern), spin liquids (where the spins interact strongly but remain fluctuating down to temperatures near absolute zero) and the spin ice (a special case of the spin liquid) which is related to the problem of proton disorder in water ice. Little is known or understood about these unusual states of matter, to which much attention has been paid over the past ten years or so. The rich behaviour of frustrated materials at low temperatures is demonstrated in table (1).

Most classical frustrated models have in common that, once the leading energy term of exchange interaction has been minimized, a large ground state degeneracy remains. The Heisenberg Hamiltonian with near neighbour interactions is:

$$\mathcal{H} = \sum_{i>j} J_{ij} \mathbf{S}_i \cdot \mathbf{S}_j \tag{1.1}$$

where $J_{ij} = J$ is know as the exchange integral or coupling. In our example of a triangle of spins, this Hamiltonian can be written as:

$$\mathcal{H} = J(\mathbf{S}_3\mathbf{S}_2 + \mathbf{S}_2\mathbf{S}_1 + \mathbf{S}_3\mathbf{S}_1) = \frac{J}{2}(\mathbf{S}_1 + \mathbf{S}_2 + \mathbf{S}_3)^2 - \frac{3J}{2}\mathbf{S}^2 \tag{1.2}$$

Material	**spin type**	**spin value**	θ_{CW}	T_C	**Low T phase**
MgV_2O_4	isotrop.	1	-750	45	long range order
ZnV_2O_4	isotrop.	1	-600	40	long range order
$CdCr_2O_4$	isotrop.	3/2	-83	9	long range order
$MgCr_2O_4$	isotrop.	3/2	-350	15	long range order
$ZnCr_2O_4$	isotrop.	3/2	-392	12.5	long range order
FeF_3	isotrop.	5/2	-230	20	long range order
$Y_2Mo_2O_7$	isotrop.	1	-200	22.5	spin glass
$Y_2Mn_2O_7$	isotrop.	3/2		17	spin glass
$Tb_2Mo_2O_7$	anisotr.	6 and 1		25	spin glass
$Gd_2Ti_2O_7$	isotrop.	7/2	-10	1	long range order
$Er_2Ti_2O_7$	anisotr.		-25	1.25	long range order
$Tb_2Ti_2O_7$	anisotr.		-19		spin liquid?
$Yb_2Ti_2O_7$	anisotr.		0	0.21	long range order
$Dy_2Ti_2O_7$	Ising	7.5$\rightarrow$ 1/2	0.5	1.2	spin ice
$Ho_2Ti_2O_7$	Ising	8$\rightarrow$ 1/2	1.9		spin ice

Table 1.1: A table of materials with spins on corner sharing tetrahedra. We show for each material the spin type, the spin value, θ_{CW} which indicates the strength of the magnetic interaction, the critical temperature at which the compound undergoes a phase transition, and the nature of the low temperature phase.

and the minimum energy is obtained when $\mathbf{S}_1+\mathbf{S}_2+\mathbf{S}_3=0$. The meaning of this constraint is that the frustration is shared among the bonds in the unit.

On a cubic lattice, in the presence on antiferromagnetic near neigbour interactions, as the temperature is lowered, the spin-spin interactions would eventually dominate the thermal energy, and the spins would align so as to be antiparallel to all their near neighbours, what is known as a Neél state. The ground state of such a system is unique, up to global rotations. However, on a lattice of corner sharing units- the kagomé lattice (see Fig. (1.3)), made up of corner sharing triangles in two dimensions, or the pyrochlore lattice (see Fig. (1.4)), consisting of corner sharing tetrahedrons in three dimensions, there are many ways to fit the units together, while maintaining the constraint for each individual unit.

The minimum energy state for a single tetrahedron in the presence of near-neighbour antiferromagnetic interactions (Heisenberg Hamiltonian),is given, similarly to (1.2), by the requirement

$$\mathbf{S}_1+\mathbf{S}_2+\mathbf{S}_3+\mathbf{S}_4=0 \tag{1.3}$$

After satisfying this constraint,we are left with two independent degrees of freedom, which can be parameterized, for example, as in Fig. (1.5), by two

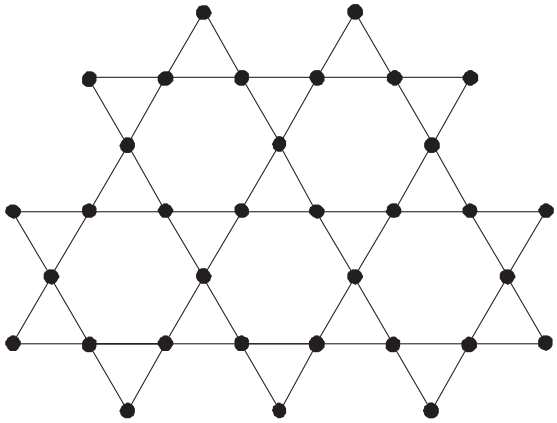

Figure 1.3: The kagomé lattice- a lattice of corner sharing triangles

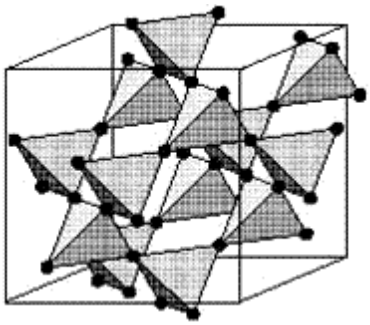

Figure 1.4: The pyrochlore lattice- a lattice of corner sharing tetrahedra

angles: α between the two planes defined by two pairs of spins, and β between two spins.

When arranging the tetrahedrons on a lattice, we impose further constraints on the spins; however,we are still left with one degree of freedom per tetrahedron. This means that each different ground state can be described by a number of continuous degrees of freedom which is proportional to the number of tetrahedral units on the lattice. This as opposed to a regular cubic ferromagnet/ antiferromagnet, where the constraints imposed by arranging cubic units on a lattice leave us with only two/four continuous degrees of freedom. Moreover, it has been shown that there are no energy barriers separating the various ground states [1].

The question that arises is, what state would such a frustrated system select at low temperatures? Effectively, since the main interaction term in the Hamiltonian does not restrict us to a single state, the ground state of the frustrated system is selected by lower order terms in the hamiltonian, such as next-near neighbor interactions, anisotropy, and entropic or quantum fluctua-

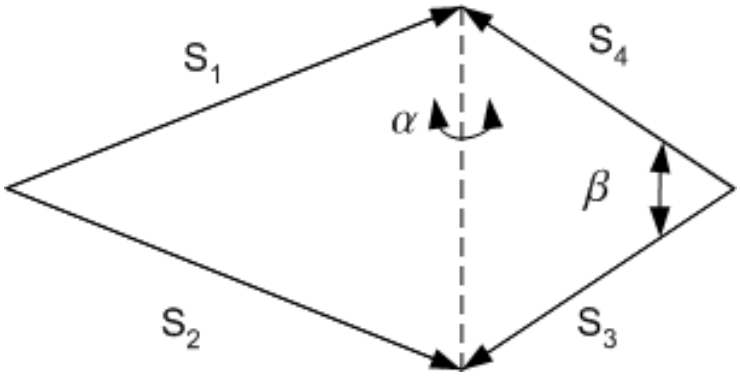

Figure 1.5: Four spins that satisfy $\mathbf{S}_1 + \mathbf{S}_2 + \mathbf{S}_3 + \mathbf{S}_4 = 0$

tions, what is known as classical[2, 3] or quantum order by disorder. Another possibility would be to add to the Hamiltonian a spin-lattice interaction that allows the lattice to distort, and thus lower its symmetry and relieve the large ground state degeneracy [4, 5, 6, 7].

Lifting of the ground state degeneracy by lattice distortion was first discussed by K. Terao [4], who examined the frustrated spin system in YMn_2, which exhibits a cubic to tetragonal phase transition. In this system the Mn ions form a pyrochlore lattice. Terao treated the spin system clasically, and examined how the lattice distortion affected the ordering of the frustrated spin system, by means of a perturbational calculation in which the distance dependence of J was taken into account within first order in the distortion. He assumed a uniform distortion for all tetrahedrons in the lattice (either elongation or shortening along the [001],[110] or [111] directions), and obtained two possible ground states, depending on the sign of the derivative of the exchange interaction J.

The quantum limit of the problem was tackled by Yamashita and Ueda [5], who started from a spin 1 Heisenberg model on corner sharing tetrahedra. They broke up each spin into a pair of 1/2-spins, and found that upon assuming an interaction between the lattice and spin degrees of freedom, the twofold degeneracy of the spin singlets on a tetrahedron was lifted by a Jahn-Teller mechanism, which led to a cubic to tetragonal phase transition. The authors proposed their model as an explanation for the cubic to tetragonal phase transition observed in the spinels ZnV_2O4 and MgV_2O_4 [8, 9].

Building on the work of Yamashita and Ueda [5], Tchernyshyov,Moessner and Sondhi [6, 7] showed that a lattice distortion can also be obtained in the classical limit of spins on a network of corner sharing tetrahedra. They added an elastic coupling of the spins to the lattice- a magnetoelastic term -to the Heisenberg Hamiltonian, balanced by an elastic energy term, and analyzed

the new minimum energy state of a single tetrahedron. They demonstrated that the tendency of individual tetrahedra to deform induced a coherent distortion of the entire crystal.

1.1 The Theory of Magnetoelastic Distortion

In this section we will show how it is possible to lower the lattice energy through a distortion which lowers its symmetry, following the idea developed by Tchernyshyov,Moessner and Sondhi [6, 7]. The hamiltonian of four spins on a tetrahedral "molecule" is given by

$$H_0 = J \sum_{i>j} \mathbf{S}_i \cdot \mathbf{S}j = \frac{J}{2}(\mathbf{S}_1 + \mathbf{S}_2 + \mathbf{S}_3 + \mathbf{S}_4)^2 - 2J\mathbf{S}^2 \tag{1.4}$$

It can be easily seen that in the ground state, the total spin on such a "molecule" is 0. We will consider classical spins ($S \to \infty$), for which the degeneracy of the ground state becomes infinite, and the ground states can be parameterized by two continuous variables- the angle between two spins, and the angle defined by the two planes containing each a pair of spins, as shown in Fig. (1.5).

We model the crystal field which keeps the ions in place by a harmonic term which depends on the distance between two ions, similar to springs connecting the spins (see fig. (1.6).

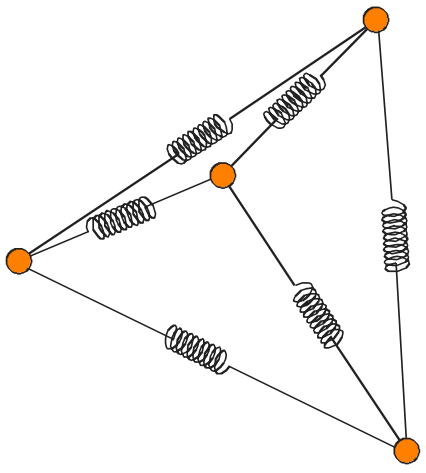

Figure 1.6: A tetrahedron in which the atoms in the corners are connected by springs.

The harmonic Hamiltonian of such a system would be:

$$H_{harmonic} = \frac{1}{2}k\sum(\delta r_{ij})^2 = \frac{1}{2}k\sum_{i>j}\left(|\mathbf{r}_i + \delta\mathbf{r}_i - \mathbf{r}_j - \delta\mathbf{r}_j| - |\mathbf{r}_i - \mathbf{r}_j|\right)^2 \quad (1.5)$$

where $i, j = 1..4$, δr_{ij} is the change in the length of the bond between atoms i and j, $\mathbf{r}_i$ denotes the location of atom i and $\delta\mathbf{r}_i$ is the change in the location of atom i. If we expand δr_{ij} to first order in all coordinates, we obtain an expression of the form:

$$H_{harmonic} \simeq \sum_{a>b}\frac{k_{ab}}{2}\delta r_a \delta r_b \quad (1.6)$$

Here δr_b denotes the change in the cartesian coordinates (δx_b,δy_b,δz_b) of atom b, so that $a, b = 1...12$.

Assuming that the exchange interaction depends on the distance between two spins, we add to the Hamiltonian a magnetoelastic term which encourages spins to grow closer/more distant depending on their relative orientation and the sign of the derivative of the exchange, given by :

$$H_{magnetoelastic} = \sum_{i>j} J'(\mathbf{S}_i \cdot \mathbf{S}_j)\delta r_{ij} \quad (1.7)$$

where J' is the change in the exchange interaction that results from a change in bond length. Again, expanding to first order in all coordinates:

$$H_{magnetoelastic} = \sum_{a>b,i>j} J'_{ab}(\mathbf{S}_i \cdot \mathbf{S}_j)\delta r_a \delta r_b \quad (1.8)$$

The total energy is then given by:

$$E = E_0 + \sum_{a>b,i>j} J'_{ab}(\mathbf{S}_i \cdot \mathbf{S}_j)\delta r_a \delta r_b + \sum_{a>b}\frac{k_{ab}}{2}\delta r_a \delta r_b \quad (1.9)$$

where

$$E_0 = J\sum_{i>j}\mathbf{S}_i \cdot \mathbf{S}j \quad (1.10)$$

Since the potential energy matrix k_{ab} is, in general, non-diagonal, it is convenient to diagonalize it and thus obtain the tetrahedron vibrational normal modes, and to express J'_{ab} in the same basis. In the new basis we no longer have mixed expressions of the form $\delta r_a \delta r_b$.

The normal modes are classified into the A_1 (singlet), E (doublet) and T_2 (triplet) representations. The singlet mode uniformly rescales exchange

interactions on all bonds, and causes the entire tetrahedron to inflate/deflate. A component of the triplet T_2 stretches and contracts by the same amount two bonds opposite each other, and since two such bonds will be equally frustrated or satisfied in the ground state (see Fig. (1.5) for clarity; the ground state constraint forces two different pairs of spins to have the same angle between them), the contribution of this vibrational mode to the relief of the degeneracy cancels out, leaving us to deal with the singlet and doublet vibrational modes only.

The normal coordinates of the singlet (A_1) and doublet (E) representations are, respectively (see fig. (1.7) for clarity):

$$q_A = \frac{1}{\sqrt{12}}(-\Delta x_1+\Delta x_2-\Delta x_3+\Delta x_4-\Delta y_1+\Delta y_2+\Delta y_3-\Delta y_4-\Delta z_1-\Delta z_2+\Delta z_3+\Delta z_4) \tag{1.11}$$

$$q_1 = \frac{1}{\sqrt{24}}(-\Delta x_1 + \Delta x_2 - \Delta x_3 + \Delta x_4 - \Delta y_1 + \Delta y_2 + \Delta y_3 - \Delta y_4 + \\ +2\Delta z_1 + 2\Delta z_2 - 2\Delta z_3 - 2\Delta z_4) \tag{1.12}$$

$$q_2 = \frac{1}{\sqrt{8}}\left(\Delta x_1 - \Delta x_2 + \Delta x_3 - \Delta x_4 - \Delta y_1 + \Delta y_2 + \Delta y_3 - \Delta y_4\right) \tag{1.13}$$

The bilinear combinations of the spin operators, in the same representation, are given by:

$$f_A = \frac{1}{\sqrt{6}}(\mathbf{S}_1\mathbf{S}_2 + \mathbf{S}_1\mathbf{S}_3 + \mathbf{S}_1\mathbf{S}_4 + \mathbf{S}_2\mathbf{S}_3 + \mathbf{S}_2\mathbf{S}_4 + \mathbf{S}_3\mathbf{S}_4) \tag{1.14}$$

$$f_1 = \frac{1}{\sqrt{12}}\left(\mathbf{S}_1\mathbf{S}_3 + \mathbf{S}_2\mathbf{S}_3 + \mathbf{S}_2\mathbf{S}_4 + \mathbf{S}_1\mathbf{S}_4 - 2\mathbf{S}_1\mathbf{S}_2 - 2\mathbf{S}_3\mathbf{S}_4\right) \tag{1.15}$$

$$f_2 = \frac{1}{2}\left(\mathbf{S}_1\mathbf{S}_3 - \mathbf{S}_2\mathbf{S}_3 - \mathbf{S}_1\mathbf{S}_4 + \mathbf{S}_2\mathbf{S}_4\right) \tag{1.16}$$

The expression (1.9) for the energy then becomes:

$$E = E_0 + 2J' f_A q_A + J'\mathbf{f}\cdot\mathbf{q} + 2kq_A^2 + \frac{1}{2}kq^2 \tag{1.17}$$

Where $\mathbf{f} = (f_1, f_2)$, $\mathbf{q} = (q_1, q_2)$. We use here the same J' and k for both representations, the difference between the representations is included in the factors of two multiplying the different terms.

Simple minimization of the energy gives:

$$\frac{\partial E}{\partial q_a} = 2J' f_A + 4k q_A = 0 \Rightarrow q_A = -J' f_A / 2k \tag{1.18}$$

$$\frac{\partial E}{\partial q} = J' \mathbf{f} + k\mathbf{q} = 0 \Rightarrow \mathbf{q} = -J' \mathbf{f}/k \tag{1.19}$$

Substituting (1.19,1.18) into (1.17) gives:

$$E_{min} = E_0 - \frac{J'^2 (f_A^2 + f^2)}{2k} \tag{1.20}$$

We therefore see that by enabling the tetrahedron to distort through the addition of a magnetoelastic spin-lattice coupling, we obtain a lower energy state than for the undistorted tetrahedron. The magnitude of the distortion depends on the angles between spins (given by f_A,$\mathbf{f}$) and on the magnetic and elastic constants J', k.

What would be the optimal value of $f = |\mathbf{f}|$? From the expression for the minimum energy it is obvious that f has to be maximal. Using (1.15) and the constraint (1.3) it can be shown that the maximal value of f for a tetrahedron is obtained when all the spins in the tetrahedron are aligned along the same axis, with two pairs of spins parallel and four pairs of spins antiparallel[7]. This also determines the value of f_A. In this state,

$$\mathbf{f} = (4/\sqrt{3}, 0)$$

and

$$f_A = 2/\sqrt{6}$$

which give us an expected value of the minimal energy per tetrahedron:

$$E_{min} = -(J + \frac{3J'^2}{2k}) \tag{1.21}$$

It is important to emphasize here the hidden assumptions of this model. Firstly, it is assumed that the ground state in the presence of a magnetoelastic distortion still has zero net spin on each tetrahedron. Secondly, it is assumed that the distortion is very small, so that it can be described by the normal vibrational coordinates of a tetrahedron, which are obtained from a first order expansion in all coordinates.

1.1.1 The $q = 0$ Distortion

How do we arrange these distorted tetrahedrons to form a lattice? O. Tchernyshyov proposed [7] a ground state for the pyrochlore lattice, in which the distortion is caused by a $\mathbf{q} = 0$ phonon, meaning that all tetrahedra with the same orientation distort in the same way. Since there are two possible orientations for the tetrahedra on the pyrochlore lattice, there are two $\mathbf{q} = 0$ possible distortions: one in which all the tetrahedra distort in the same way, and one in which the distortion alternates between layers of tetrahedra.

We present here a distortion similar to the simple uniform distortion presented by Tchernyshyov. However, Tchernyshyov chose to normalize the component of the singlet normal mode within the exchange coupling J, and to ignore the contribution of the triplet normal mode; we choose to take into account the value of the singlet component, and to set to zero the triplet component in order to obtain a symmetric distortion. What we call the $\mathbf{q} = 0$ distortion of the lattice is obtained by distorting all tetrahedrons according to:

$$q_A = -J'/\sqrt{6}k \tag{1.22}$$

$$\mathbf{q} = (-\frac{4J'}{\sqrt{3}k}, 0) \tag{1.23}$$

This means that, according to (1.11-1.13):

$$\frac{X + Y - 2Z}{\sqrt{6}} = -\frac{4J'}{\sqrt{3}k} \tag{1.24}$$

$$\frac{X - Y}{\sqrt{2}} = 0 \tag{1.25}$$

$$\frac{X + Y + Z}{\sqrt{3}} = -J'/\sqrt{6}k \tag{1.26}$$

where we adopted a visually simpler notation for the normal coordinates, in which $X = (-\Delta x_1 + \Delta x_2 - \Delta x_3 + \Delta x_4)/2$,$Y = (-\Delta y_1 + \Delta y_2 + \Delta y_3 - \Delta y_4)/2$, and $Z = (-\Delta z_1 - \Delta z_2 + \Delta z_3 + \Delta z_4)/2$.

From the three equations (1.24,1.25,1.26) we obtain:

$$X = Y = \frac{-J'}{\sqrt{2}k}$$

$$Z = \frac{3J'}{\sqrt{2}k} \tag{1.27}$$

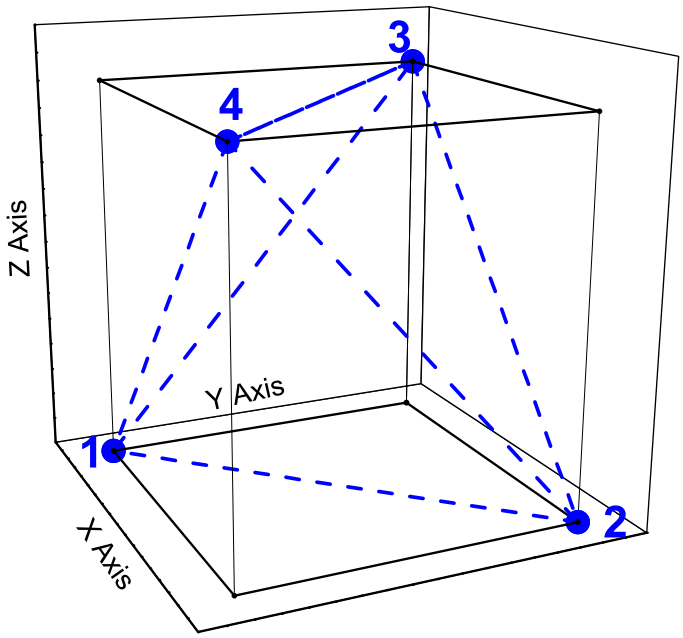

Figure 1.7: The undistorted tetrahedron

This has to be translated into shifts in the locations of individual atoms. Let's look first at the tetrahedron located at the origin of coordinates:

The solutions (1.27) we obtained for X,Y,Z give us the elongations of the tetrahedron along the three axes; they depend on the sign of J'. Assuming a negative J', the tetrahedron stretches in the x,y directions and shrinks in the z direction. This can be obtained without moving the atom at the origin. The atom numbered (2) will move in the positive x and y directions; the atom numbered (3) will move in the positive y and negative z directions; and the atom numbered (4) will move in the positive x and negative z direction. To sum it up:

$$\Delta x_1 = 0 \quad \Delta y_1 = 0 \quad \Delta z_1 = 0 \tag{1.28}$$

$$\Delta x_3 = 0 \quad \Delta y_4 = 0 \quad \Delta z_2 = 0 \tag{1.29}$$

Substituting (1.28) into the expressions for X,Y,Z we obtain:

$$(\Delta x_2 + \Delta x_4)/2 = \frac{-J'}{\sqrt{2}k}$$

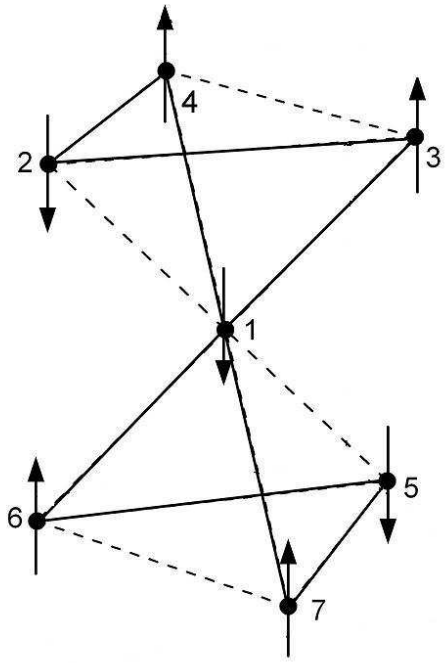

Figure 1.8: Distorted tetrahedrons. The lengthened bonds are represented by a dotted line and the shortened bonds by a continuous line.

$$(\Delta y_2 + \Delta y_3)/2 = \frac{-J'}{\sqrt{2}k}$$
$$(\Delta z_3 + \Delta z_4)/2 = \frac{3J'}{\sqrt{2}k} \tag{1.30}$$

Since we want a symmetric distortion (this actually means that we set the triplet vibrational mode equal to zero) :

$$\Delta x_2 = \Delta x_4 = \frac{-J'}{\sqrt{2}k}$$
$$\Delta y_2 = \Delta y_3 = \frac{-J'}{\sqrt{2}k}$$
$$\Delta z_3 = \Delta z_4 = \frac{3J'}{\sqrt{2}k} \tag{1.31}$$

Eq. (1.31) gives us the shift from the initial location of the atoms in a tetrahedron. When $J'/k \to 0$, we obtain the undistorted lattice again. In

Fig. (1.8) we show two distorted tetrahedrons. One can verify that opposite bonds, such as 1-2 and 1-5 ,have the same length, and that spins corresponding to such bonds have the same relative orientation, such that the forces on each atom balance to zero.

For clarity, we show in Fig. 1.9 the $q = 0$ distortion for several neighbouring tetrahedrons on the pyrochlore lattice.The lengthened bonds are represented by a dotted line and the shortened bonds by a continuous line.

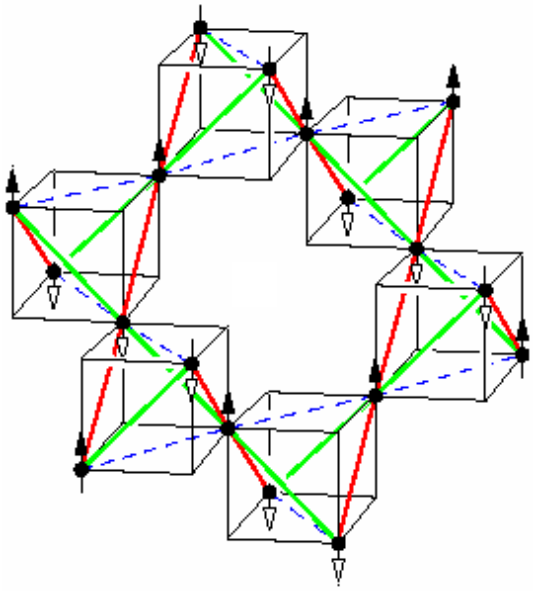

Figure 1.9: The q=0 distortion we implemented on the pyrochlore lattice. Tetrahedrons of both orientations distort in the same way.

1.2 Experimental Review

1.2.1 Characteristics of $Y_2Mo_2O_7$

$Y_2Mo_2O_7$ belongs to the cubic pyrochlores $A_2B_2O_7$, where both the A and B sublattices reside on networks of corner sharing tetrahedra. $Y_2Mo_2O_7$, with a molar mass of 481.69 gr/mol, crystallizes in an fcc structure containing eight formula units per conventional unit cell, with space group $Fd\overline{3}m$. The ions on the 16d site form a network of corner sharing tetrahedra; the 16c sites constitute an identical sublattice, displaced by $(\frac{1}{2}, \frac{1}{2}, \frac{1}{2})$. Mo^{4+} ions occupy the 16c site, while Y^{3+} ions occupy the 16d site. The spin 1 Mo^{4+}, the source of magnetism in $Y_2Mo_2O_7$, has an effective magnetic moment of $2.55\mu_B$, close to the value of $g\sqrt{S(S+1)}\mu_B = 2.8\mu_B$ expected for its value of spin [10]. The moments interact antiferromagnetically, via superexchange, giving rise to $\theta_{CW} = -200K$ [11]. The compound is semiconducting, with a band gap of $0.013eV$ [12], and exhibits a spin-glass (SG) magnetic transition at $T_g = 22.5K$, as seen from irreversible behavior in the bulk magnetic susceptibility [13], and from a rapid slowing down and freezing of the magnetic moments with no long range order down to $\sim 0.1T_g$, as seen in neutron scattering and μSR data [10, 14].

1.2.2 Frustration Driven Distortion in $Y_2Mo_2O_7$

There are more than a few experiments supporting the concept of frustration driven distortion in $Y_2Mo_2O_7$. This compound exhibits a SG transition, and theoretical calculations have long asserted that such a transition is only possible when both frustration and disorder (in the form of a distribution of exchange couplings) are present [15]. This motivated the search for lattice disorder in $Y_2Mo_2O_7$. Booth et al. [16] show, using the x-ray-absorption fine-structure technique, that the Mo tetrahedra are in fact disordered from their ideal structure, with a relatively large amount of pair distance disorder, between 0.1 and $0.2A^0$, in the $Mo-Mo$ pairs and perpendicular to the $Y-Mo$ pairs.

Keren and Gardner's[17] ^{89}Y NMR investigation of $Y_2Mo_2O_7$, also showed a broadening and shifting of the NMR spectrum upon cooling, starting at temperatures as high as $200K$. The NMR data shows well separated, regularly spaced ^{89}Y NMR peaks, which means there are many nonequivalent ^{89}Y sites, possibly stemming from a lattice distortion. In Fig. (1.10) one can see that the magnetic environment of the Y ion, which is located in the center of a Mo hexagon, would change as a result of a change in $Mo-Mo$ bond lengths.

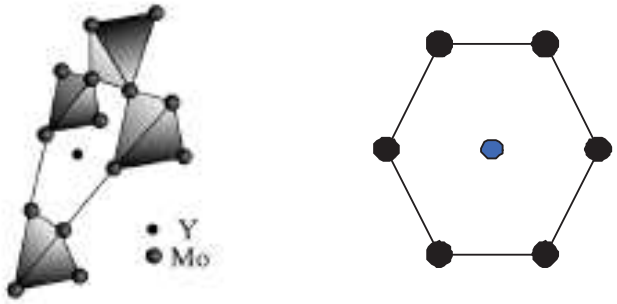

Figure 1.10: The ^{89}Y ion in the center of a Mo hexagon

Among other materials in which a lattice distortion possibly caused by frustration was observed are the spin-1 spinels ZnV_2O_4[8], MgV_2O_4[9], and the spin $\frac{3}{2}$ $ZnCr_2O_4$. In $ZnCr_2O_4$, in which the Cr^{3+} ion is ordered on a lattice of corner sharing tetrahedra, with antiferromagnetic near neighbor interactions, inelastic magnetic neutron scattering shows a first order phase transition at $T = 12.5K$, from a cubic paramagnetic material to a tetragonal lattice with Neel order [18].

1.3 Thesis Plan

We see, that experimental evidence points to both the possibilities of ordered and disordered frustration-driven distortions; it is not unreasonable to expect, in the light of the SG transition in $Y_2Mo_2O_7$, that this compound undergoes some kind of distortion that causes a distribution of exchange couplings between the magnetic ions. Since a clear cut link between experiment and theory could not be established, we took it upon ourselves to investigate, by both experimental and numerical methods, the possibility of frustration driven lattice distortion in Y_2Mo_2O. In Chapter 2 we show susceptibility and μSR experimental data which support a lattice distortion,and in Chapter 3 we further look into the theory that proposes an ordered distorted ground state for the pyrochlore lattice at $T = 0$, and in section 3.7 enquire how such a state would change at $T > 0$. Finally, in Chapter 4 we present our experimental and numerical conclusions.

Chapter 2

The Experimental Methods

2.1 Susceptibility measurements

2.1.1 Moving sample magnetometer

Let us consider a cylindrical sample of radius r and length L which moves through a coil from its upper part to its lower part and back. The dimensions of the coil are the same as the ones of the sample, and it has n turns per unit length. As the sample moves a distance dx in the coil, the field in a volume $\pi r^2 dx$ changes from H, the external field, to $B = H + 4\pi M$, where M is the sample magnetization. The change in the flux is $d\phi = n(\pi r^2)4\pi M dx$, therefore the voltage that develops in the coil is:

$$\epsilon(t) = -\frac{1}{c}\frac{d\phi}{dt} = \frac{1}{c}n(\pi r^2)4\pi M\frac{dx}{dt} \tag{2.1}$$

where c is the speed of light. The output voltage will be proportional to the sample velocity and to its magnetization.

Now lets define $S = \int_0^T |\epsilon(t)|dt$ so that

$$S = [\int_0^{T/4} \epsilon(t)dt - \int_{T/4}^{T/2} \epsilon(t)dt + \int_{T/2}^{3T/4} \epsilon(t)dt - \int_{3T/4}^{T} \epsilon(t)dt] \tag{2.2}$$

where T is the period of the motion. Using the definition of ϵ, S is also given by

$$S = \frac{1}{c}(\phi(T/4) - \phi(0) - \phi(T/2) + \phi(T/4) + \phi(3T/4) - \phi(T/2) - \phi(T) + \phi(3T/4)) \tag{2.3}$$

At times $T/4$ and $3T/4$, when the sample is in the center of the coil:

$$\phi = nBV_{sample} + nH(V_{coil} - V_{sample}) \tag{2.4}$$

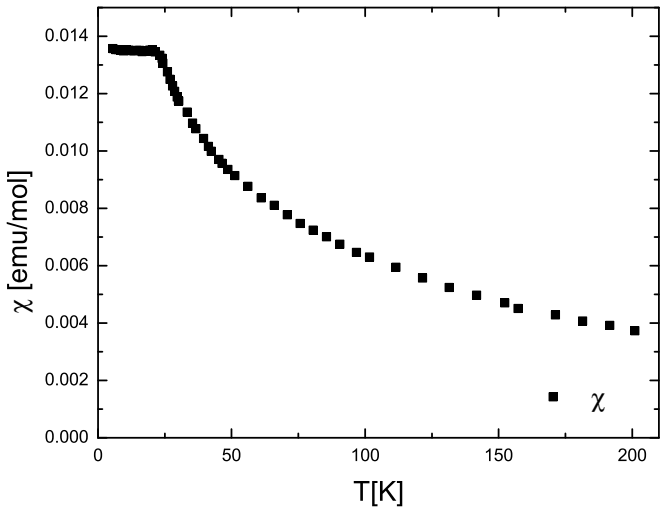

Figure 2.1: The magnetic susceptibility of $Y_2Mo_2O_7$ versus temperature in a field of $6000G$, same as the field in which the μSR experiment was performed.

At times 0, $T/2$ and T, when the sample is out of the coil, we get:

$$\phi = nHv_{coil} \tag{2.5}$$

So we get

$$S = \frac{16\pi}{c} nMV_{sample} \tag{2.6}$$

In this case the signal depends on the product of the magnetization and volume of the sample. The magnetometer is calibrated so that in the end we obtain

$$S = MV_{sample} \tag{2.7}$$

.

In order to obtain the molar susceptibility, we use

$$\chi/mol = \frac{Sm_{molar}}{Hm_{sample}} \tag{2.8}$$

We performed DC magnetization measurements on a powder sample of $Y_2Mo_2O_7$, in fields of 6000, 4000 and $2000G$. In Fig. (2.1) we can see the magnetic susceptibility of $Y_2Mo_2O_7$ versus temperature measured upon

cooling in a field of $6000G$. The freezing of spins that accompanies the SG transition can be clearly seen from the remanent component of magnetization below the transition temperature.

As temperature decreases, an increasing number of spins becomes aligned in the direction of the applied magnetic field, as can be seen from the increasing magnetization. As we shall see, at the SG transition, the spins freeze in a random configuration and the magnetization remains constant.

2.2 The μSR Experiment

μSR, which stands for muon spin relaxation, resonance, rotation or whatever, is an experimental technique that uses the spin $\frac{1}{2}$ of the muon in order to probe magnetic fields in matter. The muon is a lepton, similar to the electron, but with a mass 250 times larger and with a gyromagnetic ratio $\gamma_\mu = \frac{ge}{2m_\mu} = 2\pi \times 135.5 MHzT^{-1}$. Two features of the muon make it an ideal internal magnetic probe: muons can be produced almost 100% spin polarized, and they have a lifetime of about 2.2 μsec, after which the positive (negative) muon disintegrates into a positron (electron) and two neutrino. The positron (electron) is emitted preferentially in the direction of the muon spin at the moment of disintegration. By detecting the positron (electron) emitted, it is possible to deduce the evolution of the muon spin.

Muons are produced from the decay of pions, which have a lifetime of about $26nsec$, in the following reaction:

$$\pi^+ \rightarrow \mu^+ + \nu_\mu$$

Pions are spin zero particles, whereas neutrinos and muons both have spin half. Therefore momentum and angular momentum conservation in the rest frame of the pion require that the muon and neutrino be emitted with opposite momenta and spins. Since neutrinos are left handed particles, having momentum always opposite to spin direction, the muons must be produced with spin antiparallel to their momentum. By selecting muons from pions that decay at rest it is possible to produce a muon beam 100% polarized.

In order to probe magnetic fields in matter, energetic positive muons are implanted into a sample, where they lose kinetic energy through Coloumbic interactions, thus preserving their initial spin direction. Negative muons are not suitable for this purpose, since they would behave as heavy electrons and be trapped in low atomic orbits, interacting mainly with the nuclear spins. On the other hand, positive muons are attracted by areas of large electronic density, and stop in interstitial sites in crystals, where their polarization

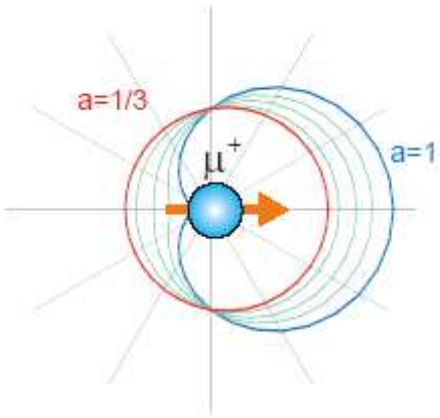

Figure 2.2: A plot of the angular distribution of emitted positrons

evolves under the effect of the magnetic fields. The slowing down of the muons occurs quickly enough to enable them to spend most of their lifetime at a single site. Moreover, only the initial part of the muon path suffers much radiation damage from the incoming muon, and the muon usually stops well away to sample a unharmed environment.

The muon decays into two neutrino and a positron:

$$\mu^+ \rightarrow e^+ + \nu_e + \bar{\nu}_\mu$$

Again, this decay involves two left handed particles, the neutrino, whose momentum must be antiparallel to their spin. Momentum and angular momentum conservation considerations (the decay occurs with the muon at rest, therefore it is enough to consider the problem in the rest frame of the muon), lead to a propensity for the emitted positron to be emitted preferentially along the direction of the muon spin. The angular distribution of emitted positrons depends on their energy, and is given by (see Fig. (2.2)):

$$W(\theta, \epsilon) = 1 + a(\epsilon) cos\theta$$

where ϵ is the positron energy and θ the angle between the direction of the muon spin and the positron momentum. a is the asymmetry parameter, which depends on the energy of the detected positron , and ranges between $-\frac{1}{3}$ for $\epsilon = 0$ and 1 for $\epsilon = \epsilon_{max}$ (which is achieved when both neutrino are emitted in the same direction). When all positron energies are sampled with equal probability, the value of the asymmetry parameter a is $\frac{1}{3}$.

By detecting positrons emitted from a large number of muons implanted in the sample to be studied, one can determine the statistical average direction of the spin polarization of the muon ensemble. The time evolution of

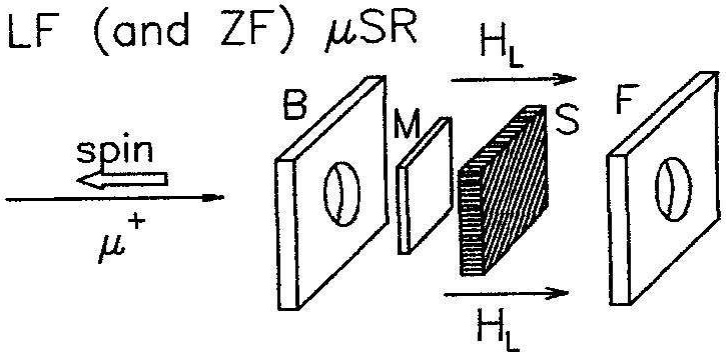

Figure 2.3: Longitudinal field experimental setup

the muon polarization depends sensitively on the dynamic fluctuations and spatial distribution of the magnetic fields in the sample.

2.3 The Experimental Setting

μSR experiments are usually performed in a magnetic field, in one of two conventional configurations:

- LF (Longitudinal Field) configuration, in which the external magnetic field is parallel to the muon beam and to the initial muon spin direction. In this configuration we detect positrons emitted in the forward and backward direction relative to the initial muon spin direction, and measure the rate at which the muon loses its initial polarization in the longitudinal direction. This measurement can also be performed with zero applied field, thanks to the initial polarization of the muon beam.

- TF (Transverse Field) configuration, in which the external magnetic field is applied perpendicular to the muon beam and the positrons are collected by counters above, below and to the sides of the initial muon beam direction. This configuration serves to measure both the frequency of muon precession and the rate at which the muons dephase due to static and dynamic field inhomogeneity.

With the aid of an electronic system, each positron detector supplies a histogram of detected positrons as a function of the time difference between a

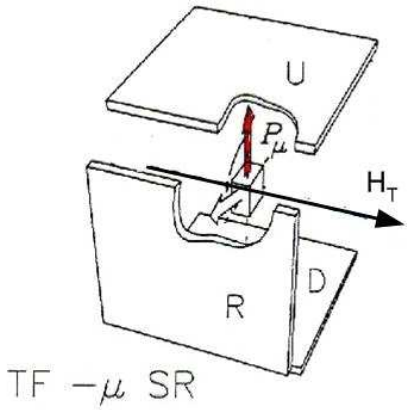

Figure 2.4: Transverse field experimental setup

muon's arrival in the sample and its decay. The number of detected positrons in a histogram corresponding to the i_{th} counter is given by:

$$N_i(t) = N_i^0 e^{-t/\tau_\mu}[(1 + A_i^0 P_i(t))] + Bg_i \tag{2.9}$$

Where Bg_i is a time independent background (coming, from example, from a fraction of muons that decay outside of the sample),N_i^0 is a normalization constant which restricts $N_i(t) \in [0, 1]$, $P_i(t)$ is the muon polarization function as seen by the counter and A_i^0 is the asymmetry.

Our experiment was performed at the GPS (General Purpose Surface Muons) instrument at PSI. The muon beam there consists of positive muons originating from the decay of positive pions at rest, and thus the spin of the muons points in the direction of their momentum. The PSI muon source is a CW (continuous wave) source, and it produces muons that arrive at the instrument without any distinct time structure. Therefore, consecutive muon decay events must be rejected over periods of time long compared to the muon lifetime, in order to avoid ambiguity in relating a decay positron to its parent muon. In CW μSR each individual muon and its decay positron are individually counted.

The beamline is equipped with a spin rotator which allows us to rotate the muon-spin direction with respect to the muon momentum. The detector arrangement consists of a muon detector M, five positron detectors (with respect to the beam direction): Forward, Backward, Up, Down, and Right (denoted FBUDR respectively), and a backward veto detector, which collimates the muon beam and rejects muons and decay positrons which miss the aperture. The muons are implanted into the sample one by one, and a logical circuit records the time at which a positron is detected, and ensures that it

corresponds to a muon that entered the sample at $t = 0$. The magnetic field at the sample location is generated along the muon beam direction, and TF measurements are performed with the muon spin rotated by the spin rotator. In this geometry, the spin rotator rotates the spin upward by about 50^0. When a transverse field is applied, the detectors U,D,R have a reduced asymmetry corresponding to the projection of the polarization vector along the direction perpendicular to the muon beam direction.

The instrument's geometry enabled us to perform simultaneous LF and TF measurements. With the muon spin tilted by 50^0 relative to the direction of magnetic field applied, the initial beam polarization has components both perpendicular and parallel to the magnetic field applied. We collected data simultaneously at the five positron detectors; the UDR positron counters collected TF data, whereas the FB counters collected longitudinal depolarization data. We measured a powder sample of $Y_2Mo_2O_7$ at temperatures ranging between 20^0K and 240^0K, in a magnetic field of $6000G$.

In the TF geometry, we record positron data with three counters, thus measuring both x and y components of the muon polarization. Ignoring geometric misalignments and differences in counter geometry, $P_y(t)$ differs from $P_x(t)$ only by a phase of $\pi/2$. Thus the muon spin polarization transverse to the magnetic field may be described by the complex quantity $P(t) = P_x(t) + iP_y(t)$, and the complex asymmetry for this counter setup is:

$$A(t) = A_0P(t) = A_0[P_x(t) + iP_y(t)] = A_x(t) + iA_y(t) \tag{2.10}$$

using (2.9) we get for the corrected TF asymmetry:

$$A_i(t) = e^{t/\tau_\mu}[\frac{N_i(t) - Bg_i}{N_i^0}] - 1 \tag{2.11}$$

In terms of the individual counters, the real asymmetry $A_x(t)$ and the imaginary asymmetry $A_y(t)$ can be written:

$$A_x(t) = \frac{1}{2}[A_U(t) - A_D(t)] \tag{2.12}$$

$$A_y(t) = A_R(t) \tag{2.13}$$

It is convenient to fit the measured asymmetry in a rotating reference frame (RRF):

$$Rel(t) = A_x(t)cos(\omega_{RRF}t) + A_y(t)sin(\omega_{RRF}t) \tag{2.14}$$

$$Img(t) = -A_x(t)sin(\omega_{RRF}t) + A_y(t)cos(\omega_{RRF}t) \tag{2.15}$$

The *Rel* and *Img* components represent our signal in the rotating reference frame, at instances of rotation with a phase difference of $\pi/2$ between them. If we take the *RRF* frequency to be slightly lower than the average Larmor-precession $\overline{\omega}_\mu = \gamma_\mu H_{TF}$ of the muon, the precession signal viewed in this rotating reference frame has only low frequency components of order $\overline{\omega}_\mu - \omega_{RRF}$. This has two advantages- it enables us to visually inspect the quality of the fit, and it allows the data to be packed into fewer bins, enhancing the speed of fitting.

In the LF geometry, the data is recorded with the F and B counters. The raw experimental asymmetry for this counter setup is defined as:

$$A_r(t) = \frac{[N_B(t) - Bg_B] - [N_F(t) - Bg_F]}{[N_B(t) - Bg_B] + [N_F(t) - Bg_F]} \tag{2.16}$$

therefore

$$A_r(t) = \frac{N_B^0[1 + A_B^0 P_B(t)] - N_F^0[1 + A_F^0 P_F(t)]}{N_B^0[1 + A_B^0 P_B(t)] + N_F^0[1 + A_F^0 P_F(t)]} \tag{2.17}$$

The phase difference between the B and F counters is of 180^0 so that

$$P_B(t) = -P_F(t) = P(t) \tag{2.18}$$

and assuming $A_B^0 = A_F^0 = A^0$ (2.17) becomes:

$$A_r(t) = \frac{(N_B^0 - N_F^0) + (N_B^0 - N_F^0)A^0 P(t)}{(N_B^0 + N_F^0) + (N_B^0 - N_F^0)A^0 P(t)} \tag{2.19}$$

It is customary to define a parameter α to be the ratio of raw count rates:

$$\alpha = \frac{N_0^F}{N_0^B} \tag{2.20}$$

Then the corrected asymmetry for a two detector setup is given by:

$$A(t) = A^0 P(t) = \frac{(\alpha - 1) + (\alpha + 1)A_r(t)}{(\alpha + 1) + (\alpha - 1)A_r(t)} \tag{2.21}$$

and in terms of the number of counts at each detector:

$$A(t) = \frac{\alpha[N_B(t) - Bg_B] - [N_F(t) - Bg_F]}{\alpha[N_B(t) - Bg_B] + [N_F(t) - Bg_F]} \tag{2.22}$$

For the purpose of data analysis we plotted both corrected LF asymmetry and TF asymmetry. The TF asymmetry in a field of $6000G$ was plotted in a rotating reference frame that corresponds to a field of $5600G$. The counters

at the GPS instrument have an asymmetry A^0 of about 0.25. Since we performed the LF experiment with the muon beam rotated by 50^0, in order to collect TF data at the same time, we expect the effective asymmetry to be the projection of the muon asymmetry upon the LF direction

$$A_e^0 = A^0 cos(50^0) = 0.16 \tag{2.23}$$

We used this assumption in order to find the α parameter for the LF data fits.

2.4 Experimental Results

We observed temperature-dependent relaxation in both the TF and LF runs. The relaxation, which is almost nonexistent above 60^0K, increases towards low temperatures, and peaks below the phase transition temperature. Therefore we present only data below 55^0K . In Fig. (2.5) we see the LF experiment at various temperatures, and we can see the increase in relaxation with decreasing temperature. We fit all the LF data to a root exponential:

$$A(t) = A_0 \exp(-(R_{LF}t)^{\frac{1}{2}}) + Bg \tag{2.24}$$

Where the parameters A_0 and Bg were shared by all data sets, and the relaxation rate R_{LF} was free for different data sets. Similarly, we found that the best fit for the TF data sets was an oscillating root exponential of the form:

$$A(t) = A_0 \exp(-(R_{TF}t)^{\frac{1}{2}}) cos(\omega t + \phi) + Bg \tag{2.25}$$

Here also we shared the initial asymmetry A_0, the rotation frequency ω, and the background Bg. The relaxation rate R_{TF} and the phase ϕ were free to change between data sets. The fact that a single frequency could fit all data sets with no shift is surprising and will be discusses later. The fits were done with the advanced fitting tool available in Origin. The LF fits were performed simultaneously to ensure parameter matching, whereas the TF parameters were set using the highest temperature (55^0K) data set. In Figs. (2.5,2.6) we present the fits for LF and TF data at 23.2^0K, 30.2^0K and 45.2^0K.

In a μSR experiment there are two mechanisms for relaxation:

1. Relaxation caused by dynamical field fluctuations, which exist even if the static field distribution has zero width, and which consists of both longitudinal relaxation caused by fluctuations in the xy plane, and dynamical transverse relaxation caused by fluctuations in the z direction. This is irreversible relaxation, which involves an energy transfer between the spin system and a heat bath (the lattice).

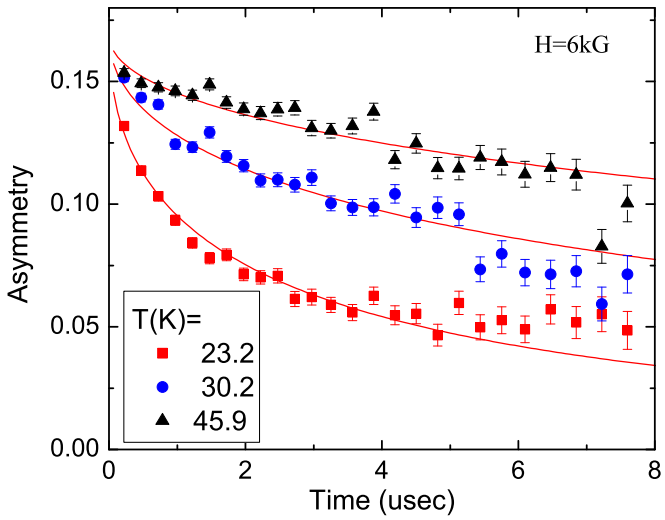

Figure 2.5: Longitudinal field asymmetries for 23.2^0K, 30.2^0K and 45.2^0K. The solid line is the fit to root exponential.

2. Static relaxation, which is reversible. It is caused by field inhomogeneities in the sample ΔB which are responsible for dephasing in the xy plane.

The relaxation in the TF experiment consists of dynamic relaxation as well as dephasing caused by a random static field distribution. Our aim is to isolate the static component of the relaxation, in order to deduce the distribution of magnetic fields in the sample, and see whether a lattice distortion occurs under the influence of the large geometric frustration present in $Y_2Mo_2O_7$. This could be done using the LF measurements to find the dynamic relaxation rate, and subtract it from the TF relaxation rate. However, this should be done carefully. The LF relaxation is caused by dynamical fluctuations in the xy directions. The dynamic contribution to the relaxation in the TF experiment (from a RRF point of view) is from fluctuations in the two directions perpendicular to the spins (out of which one is the original z direction). Assuming fluctuations in all directions are the same, and based on the fit results, we expect the following relation

$$P_0 \exp(-(R_{TF}t)^{1/2})cos(\omega t) = \exp(-(R_{LF}t)^{1/2})P_{static}(t)$$

since when the relaxation is a result of two different mechanisms, the relaxation function is a product of the individual polarization functions. There-

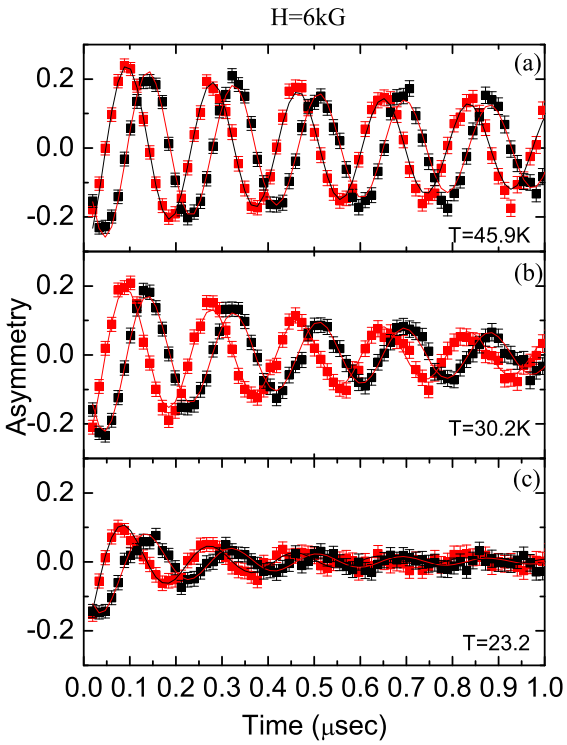

Figure 2.6: Transverse field asymmetries for 23.2^0K, 30.2^0K and 45.2^0K. The solid line is the fit to root exponential.

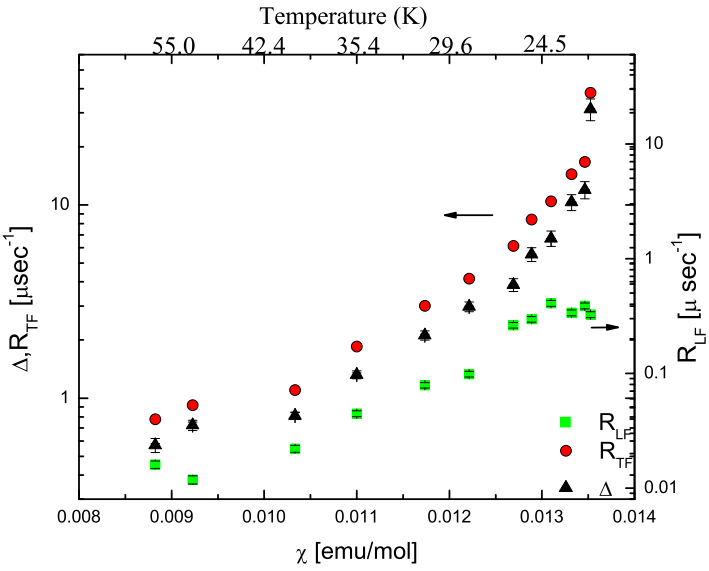

Figure 2.7: A plot of Δ and both longitudinal and transverse relaxation rates versus susceptibility and temperature.

fore, the muon polarization under the influence of static internal fields only is given by:

$$P_{static}(t) = P_0 \exp(-(\Delta t)^{1/2}) cos(\omega t) \tag{2.26}$$

Where

$$\Delta = [R_{TF}^{1/2} - R_{LF}^{1/2}]^2 \tag{2.27}$$

and

$$\omega = \gamma_\mu H_{TF} \tag{2.28}$$

In a μSR experiment, we expect an increase in the relaxation that originates from static fields as temperature is lowered, simply because in a magnetic field, the static component of magnetization increases as the energy required to flip a spin exceeds the thermal energy. This increase in the average magnetic moment of the compound is seen in the susceptibility measurements. The relation between the static μSR relaxation rate and susceptibility will show us if there are additional sources for static relaxation; if the rate of increase in μSR relaxation exceeds the rate of increase of susceptibility, it means that as temperature is lowered, additional relaxation sources appear.

In Fig. (2.7) we plotted R_{TF}, R_{LF}, Δ on a log scale vs. T and χ (with T as implicit parameter) on the upper and lower abscissa respectively. From

this figure we see that the dynamical correction to the relaxation is insignificant at low temperatures. It is also clear that Δ is not a linear function of the susceptibility χ. In fact, Δ grows exponentially fast with increasing χ, with the change in the growth rate taking place well before the SG phase transition.

2.5 Discussion of Experimental Results

Next, we would like to connect this static relaxation rate Δ to the coupling of the muon to its electronic neighbors, as well as to the sample's magnetic susceptibility. The muon Hamiltonian is:

$$H = \gamma_\mu \mathbf{I} \cdot (\mathbf{H}_{TF} + \mathbf{H}_{int}) \tag{2.29}$$

where $\mathbf{I}$ is the spin of the muon, and $\mathbf{H}_{int}$ is the magnetic field from the neighboring electrons, given by:

$$\mathbf{H}_{int} = \sum_j A_j \mathbf{S}_j \tag{2.30}$$

$A_j = A_j(\mathbf{r})$ is the coupling between the muon and electron spins, $\mathbf{S}_j$ is the electrons' spin and j is an index that runs over the muon's neighboring electrons. Applying a mean field approximation, we replace $\mathbf{S}$ by its expectation value: $< \mathbf{S} >= \mathbf{M} = \chi \mathbf{H}$. Therefore, the muon experiences a magnetic field:

$$\mathbf{B} = (1 + \sum_j A_j \chi) \mathbf{H}_{TF} \tag{2.31}$$

Assuming that the susceptibility and the couplings A_j are isotropic, then the time evolution of a single muon is given by:

$$P(t) = P_0 \cos[\gamma_\mu (1 + \sum_j A_j \chi) H_{TF} t] \tag{2.32}$$

This expression has to be averaged over the distribution of the couplings, in order to give us the relaxation function measured by μSR:

$$P_{xy}(t) = \int P_0 \cos[\gamma_\mu (1 + \sum_j A_j \chi) H_{TF} t] \rho(A_i) ... \rho(A_n) dA_1 ... dA_n \tag{2.33}$$

Since the integrals over A_j distributions are independent, we can begin by assuming that the muon interacts with a single electron:

$$P_{xy}(t) = \int P_0 \cos[\gamma_\mu (1 + A\chi) H_{TF} t] \rho(A) dA \tag{2.34}$$

Using (2.26) we obtain:

$$\exp(-(\Delta t)^{1/2})\cos(\omega t) = \int_{-\infty}^{\infty} \cos[\gamma_\mu(1+A\chi)H_{TF}t]\rho(A)dA = \tag{2.35}$$

$$= \int_{-\infty}^{\infty} \left(\cos(\omega t)\cos\left(\gamma_\mu A\chi H_{TF}t\right) + \sin(\omega t)\sin\left(\gamma_\mu A\chi H_{TF}t\right)\right)\rho(A)dA =$$

$$= \cos(\omega t)\int_{-\infty}^{\infty} \cos\left(A\chi\gamma_\mu H_{TF}t\right)\rho(A)dA + \sin(\omega t)\int_{-\infty}^{\infty} \sin\left(A\chi\gamma_\mu H_{TF}t\right)\rho(A)dA$$

If $\rho(A)$ is symmetric around zero, then the sine integral vanishes and the coupling distribution is given by:

$$\exp(-(\Delta t)^{1/2}) = \int_0^{\infty} \cos\left(A\chi\gamma_\mu H_{TF}t\right)\rho(A)dA \tag{2.36}$$

To invert the relation we define:

$$T = \chi\gamma_\mu H_{TF}t \tag{2.37}$$

and obtain:

$$\exp(-(\frac{\Delta}{\chi\gamma_\mu H_{TF}}T)^{1/2}) = \int_0^{\infty} \cos\left(AT\right)\rho(A)dA \tag{2.38}$$

This is an easily inverted cosine fourier transform:

$$\rho(A) = \frac{2}{\pi}\int_0^{\infty} \exp(-(\frac{\Delta}{\chi\gamma_\mu H_{TF}}T)^{1/2})\cos\left(AT\right)dT \tag{2.39}$$

Defining an effective width for the distribution:

$$\delta A = \left|\frac{\Delta}{\chi\gamma_\mu H_{TF}}\right| \tag{2.40}$$

We have

$$\rho(A) = \frac{2}{\pi}\int_0^{\infty} \exp(-(\delta AT)^{1/2})\cos\left(AT\right)dT =$$

$$= -\frac{1}{2|A|}\sqrt{\frac{2\delta A}{\pi|A|}}\{\sin\left(\frac{\delta A}{4\,|A|}\right)\left(2\ FresnelS\left(\sqrt{\frac{\delta A}{2\pi\,|A|}}\right) - 1\right) +$$

$$+\cos\left(\frac{\delta A}{4\,|A|}\right)\left(2FresnelC\left(\sqrt{\frac{\delta A}{2\pi\,|A|}}\right) - 1\right)\} \tag{2.41}$$

where *FresnelS* and *FresnelC* are, respectively, the Fresnel sine and cosine integrals:

$$\int_0^x \sin\left(\frac{\pi}{2}t^2\right) dt; \int_0^x \cos\left(\frac{\pi}{2}t^2\right) dt \tag{2.42}$$

Hence we see that

$$\rho(A) = \frac{1}{|A|} f(\frac{\delta A}{|A|}) \tag{2.43}$$

$\rho(A)$ has some interesting mathematical properties. It is integrable, and

$$\int_0^\infty \rho\left(A\right) dA = \frac{1}{\delta A} \tag{2.44}$$

and therefore could represent a distribution. On the other hand its asymptotic expansion is given by

$$\lim_{A\to\infty} \rho(A) = \sqrt{\frac{\pi}{2}\frac{\delta A}{A^3}} - O(A^{-2}) \tag{2.45}$$

and this is a distribution without a second moment. Therefore, the distribution cannot be characterized by a line width. In Fig. (2.8) we show the shape of $\rho(A)$. The function given in eq. (2.41) diverges at zero, and oscillates around zero.

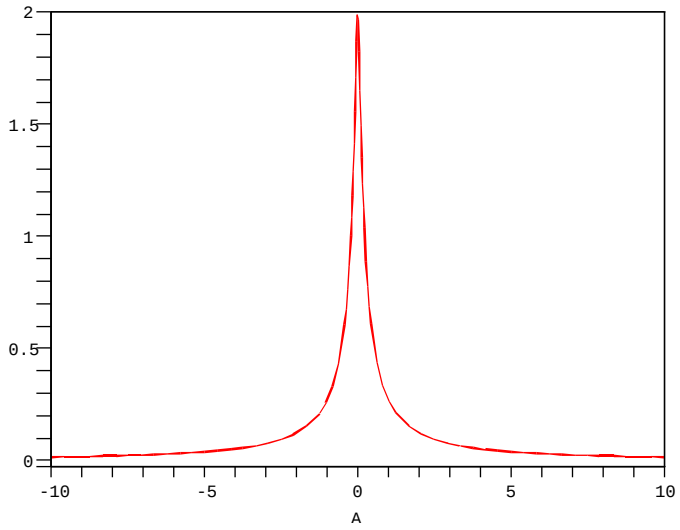

Figure 2.8: A qualitative plot of $\rho\left(\frac{1}{|A|}f(\frac{\delta A}{|A|})\right)$ as given in eq. (2.41), plotted using $\delta A = 1$.

2.6 Experimental Conclusions

The most important experimental finding is that Δ is not proportional to or even a linear function of χ. Therefore,δA given by eq. (2.40) has a temperature dependence which cannot be eliminated by subtracting a constant from Δ, χ or both. As the temperature is lowered, the ratio $\frac{\Delta}{\chi}$, and therefore δA, grows, and the distribution widens. This can only take place if atoms shift as the temperature is lowered. The fact that no change in the muon rotation frequency is detected at all temperatures means that the average coupling constant $< A >$ is always zero. However, we find no evidence for a periodic rearrangement of the atoms. We therefore move to the second part of this thesis: a numerical re-examination of the theory.

Chapter 3

Simulations

3.1 Motivation-Can We Find A Better Ground State?

In section (1.1) we surveyed theoretical work supporting a frustration-driven lattice distortion, and in section (2.4) we showed experimental evidence supporting such a distortion in $Y_2Mo_2O_7$. However, we were left with some open questions:

- How would nonharmonic terms in the Hamiltonian affect the distortion? The theory assumes that only first order terms in the distortion are kept.

- How much do we need to increase the energy of the system from the ordered distorted ground state, in order to witness disordered states? It seems that in our experiment, the distortion is of a disordered nature.

- Theoretically, the sum of spins on each tetrahedron would have to remain zero in the ground state that includes a magnetoelastic distortion, since the Heisenberg term is the leading term of the Hamiltonian. We would like to test this theoretical assumption.

In order to answer these questions,we decided to look for the ground state of the Heisenberg Hamiltonian in the presence of a magnetoelastic coupling, with the aid of a computer simulation which modelled the pyrochlore lattice with magnetic and elastic interactions.

3.2 Description of the Simulation

The coordinates of atoms in a pyrochlore lattice were stored in a three-dimensional array. For programming reasons, the axes chosen were not the conventional axes, in which the coordinates of the atoms in the first tetrahedron would be :

1. $(0, 0, 0)$
2. $(\sqrt{2}/2, \sqrt{2}/2, 0)$
3. $(0, \sqrt{2}/2, \sqrt{2}/2)$
4. $(\sqrt{2}/2, 0, \sqrt{2}/2)$

assuming interatomic distance of unity, but a rotated system of axes, with the rotation matrix given by:

$$R = \begin{pmatrix} \sqrt{2}/2 & -\sqrt{6}/6 & \sqrt{3}/3 \\ \sqrt{2}/2 & \sqrt{6}/6 & -\sqrt{3}/3 \\ 0 & \sqrt{2/3} & \sqrt{3}/3 \end{pmatrix} \tag{3.1}$$

and the coordinates of the atoms in the first tetrahedron given by:

1. $(0, 0, 0)$
2. $(1, 0, 0)$
3. $(1/2, \sqrt{3}/2, 0)$
4. $(1/2, \sqrt{3}/6, \sqrt{2/3})$

We denote the vectors pointing to atoms $2, 3, 4$ by $\mathbf{V}_1, \mathbf{V}_2, \mathbf{V}_3$ respectively. The coordinates of an atom in the lattice where given by:

$$\mathbf{X} = B\mathbf{M} \tag{3.2}$$

where

$$B = \begin{pmatrix} 1 & 1/2 & 1/2 \\ 0 & \sqrt{3}/2 & 1/\sqrt{12} \\ 0 & 0 & 2/\sqrt{6} \end{pmatrix} \tag{3.3}$$

and $\mathbf{M} = (m, n, l)$ is a vector of integers.

The choice of boundary conditions is very important. Computer simulations are usually performed on a small number of atoms, of the order of

$N = 10000$, since the size of the system is limited by the available storage on the computer and, more crucially, by the speed of execution of the program. To simulate a bulk material, which has about 10^{23} atoms, and in which most of the atoms do not experience any surface effects, it is customary to use periodic boundary conditions, in which the system under study is surrounded by mirror images of itself in each dimension, thus mimicking an infinite system [[19]]. This would be suitable for a system of spins only; for example, when looking for the minimum energy state of the Heisenberg Hamiltonian. However, periodic boundary conditions do not allow for a distortion of the crystal, since an expansion on one side would necessarily be accompanied by a shrinking of the opposite side. Therefore we chose to use open boundary conditions for the coordinates, and periodic boundary conditions for the spins, in order to minimize boundary effects on one hand, and enable a lattice distortion on the other hand. The periodic boundary conditions for the spins also ensure that we maintain spin frustration in all tetrahedra of the virtual lattice. This frustration is the most important property of the physics question under investigation. That this choice induces an acceptable error will be shown in (3.3).

The energy of the entire lattice is a function of the relative orientations and distances of near-neighboring spins. The energy minimization algorithm is based on trying a change of location and orientation for each of the spins in the lattice, and checking whether it induces a decrease or an increase on the value of the energy function for the entire lattice. To this end it is enough to check the energy change δE in the interaction of a spin with its near neighbours. Both spin and position are minimized simultaneously. The basic simulation cell contains between 8788 and 13500 atoms.

We started by minimizing the Heisenberg Hamiltonian with near-neighbor interactions:

$$H = J \sum_{i>j} \mathbf{S}_i \cdot \mathbf{S}_j \tag{3.4}$$

The spins were taken to be classical spins,namely they can have any orientation, with $|\mathbf{S}| = 1$.

The energy can then be written as:

$$E_0 = J \sum_{i>j} \mathbf{S}_i \cdot \mathbf{S}_j = \frac{J}{2} \sum (\mathbf{S}_1 + \mathbf{S}_2 + \mathbf{S}_3 + \mathbf{S}_4)^2 - NJ. \tag{3.5}$$

where N is the number of spins in the lattice, and the sum is taken over all tetrahedron units in the lattice. The energy is minimized when constraint (1.3) is fulfilled for all tetrahedrons. Thus the minimum value of the energy in the absence of the magnetoelastic coupling was expected to be $E_0 = -NJ$.

The second step was to add an energy term of the form

$$E_{J'} = \sum_{i>j}(\frac{dJ}{dr_{ij}})(\mathbf{S}_i \cdot \mathbf{S}_j)\delta r_{ij} = J' \sum_{i>j}(\mathbf{S}_i \cdot \mathbf{S}_j)\delta r_{ij} \tag{3.6}$$

where δr_{ij} denotes the change in the distance between two spins (it is important to mention that in our simulation, δr_{ij} is the actual change in the distance between spins, and not only the linearized change), and can be positive or negative, and J' was the magnetoelastic constant which determined the magnitude of the spin-lattice coupling. In fact, $F = J'\mathbf{S}_i \cdot \mathbf{S}_j$ is a repelling/attractive force which acts between two neighboring spins, and causes the distance between them to grow/decrease. The force depends on the sign of J'- a positive(negative) J' means that the AF exchange interaction increases(decreases) with distance between spins, but it also depends on the angle between spins- antiparallel(parallel) spins would favor a larger(smaller) AF exchange interaction. Since the effective exchange interaction is $J_{eff} = J + J'\delta r_{ij}$, the range of values for J' has to be chosen carefully, in order to remain in the AF regime.

To model the crystal field which determines the crystal structure, we added an elastic term

$$E_k = \frac{k}{2}\sum_{i>j}(\delta r_{ij})^2 \tag{3.7}$$

J' and k had the same value for all the bonds in the simulated lattice.

Thus the function to be minimized by the simulation is:

$$\mathcal{H} = J\sum_{i>j}\mathbf{S}_i \cdot \mathbf{S}_j + J'\sum_{i>j}(\mathbf{S}_i \cdot \mathbf{S}_j)\delta r_{ij} + \frac{k}{2}\sum_{i>j}(\delta r_{ij})^2 \tag{3.8}$$

In order to be able to compare the simulation results to theoretical values, we calculated the expected value of the minimal energy of the entire lattice using the value of the minimal energy for a single tetrahedron (1.20):

$$E_{min} = -NJ - \frac{N}{2}\frac{J'^2(f_A^2 + f^2)}{2k} = -N(J + \frac{J'^2(f_A^2 + f^2)}{4k}) \tag{3.9}$$

where N is the number of atoms in the lattice. The number of tetrahedra in the lattice, in the limit of $N \to \infty$, is given by $\frac{N}{2}$, since every atom belongs to two tetrahedra (the tetrahedra are corner-sharing), and every tetrahedron consists of four atoms.

Substituting for the minimum value of f_A and $f = |\mathbf{f}|$ we obtain

$$E_{min} = -N(J + \frac{3J'^2}{2k}) \tag{3.10}$$

The input to the simulation consisted of the initial ordering of the spins (namely the lattice structure and spin configuration), and of the values of J,J' and k, which were constant during single runs but varied between different runs of the simulation.

The final output of the computer simulation included the minimum-energy atomic locations and the orientations of the spins, as well as the changes in bond lengths, the near-neighbor spin-spin correlation $S_i \cdot S_j$, the sum of spins on a tetrahedron, and lattice statistics such as the value of the minimum energy, the average change in bond length, the average square change in bond length, and the number of bonds that become ferromagnetic as a result of the change in bond length (this to insure that we remain in the AF regime). In order to analyze the simulation results, we used a Matlab script that performed magnetic and nonmagnetic neutron scattering on the virtual lattice (see Appendices A, B), using the Laue method (fixed single crystal and various incident wavelengths).

After constructing the simulation lattice, we performed on it nonmagnetic neutron scattering, in order to ensure that it was constructed correctly. In Fig. (3.1) we show the scattering intensity vs. magnitude of the scattering vector in the [111] direction- which means that the scattering vector $\mathbf{q}$ points in the direction of the sum of the three generating vectors of the lattice: $\mathbf{q} = (\mathbf{V}_1 + \mathbf{V}_2 + \mathbf{V}_3)/|\mathbf{V}_1 + \mathbf{V}_2 + \mathbf{V}_3|$.

We see peaks at $|\mathbf{q}| \sim 7.7$ and $|\mathbf{q}| \sim 3.85$. Since we know that peaks should be obtained at $|\mathbf{q}| = 2\pi/d$, where d is the spacing between lattice planes, we easily recognize the peaks to correspond respectively to the distances between neighboring kagomé planes and triangular planes ($d = 0.816497$), and to the distances between planes of the same kind (kagomé or triangular, $d = 1.632993$).

It is also worthwhile to take a look at the magnetic scattering from a pyrochlore lattice with collinear spins that satisfy (1.3) for all tetrahedrons, as shown in Fig. (3.2). In this lattice, neighboring planes are antiferromagnetically correlated, and next-near neighbouring planes are ferromagnetically correlated; the magnetic periodicity is different from the structural periodicity of the lattice. Thus the peak corresponding to $d = 0.816497$ disappears; there is a ferromagnetic correlation between triangular planes and between kagomé planes, which we see in the $d = 1.632993$ peak.

It is important to bear in mind that, while here the magnetic and spatial parts of the scattering are separate, since they are generated by computer, in an actual experiment we would observe the two scatterings superimposed.

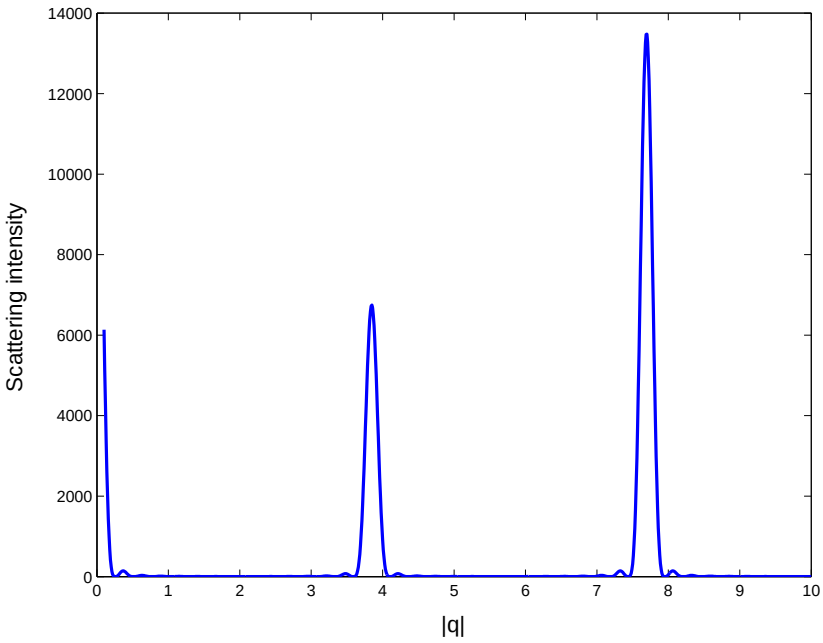

Figure 3.1: Scattering intensity vs. magnitude of the scattering vector in the [111] direction, for a pyrochlore lattice of 13500 spins.

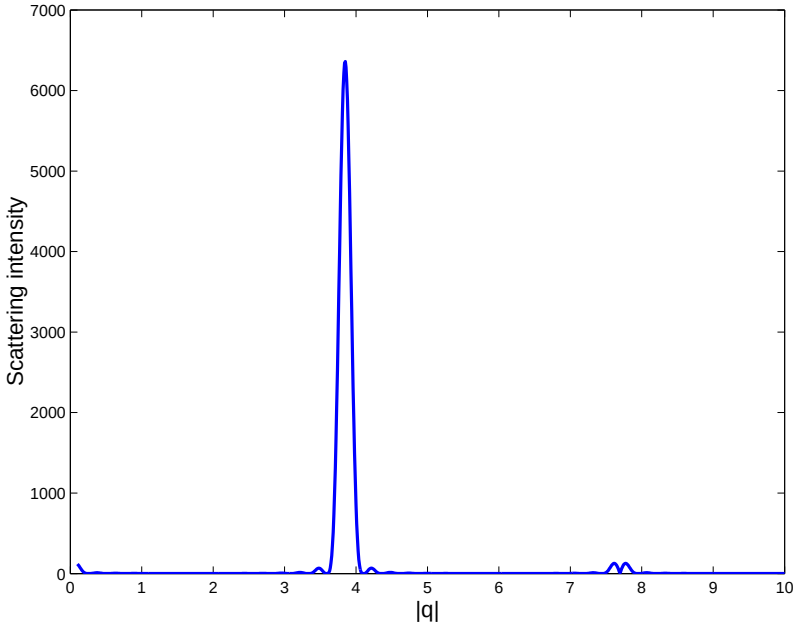

Figure 3.2: Magnetic scattering intensity vs. magnitude of the scattering vector in the [111] direction, for an AF ordered pyrochlore lattice of 13500 spins.

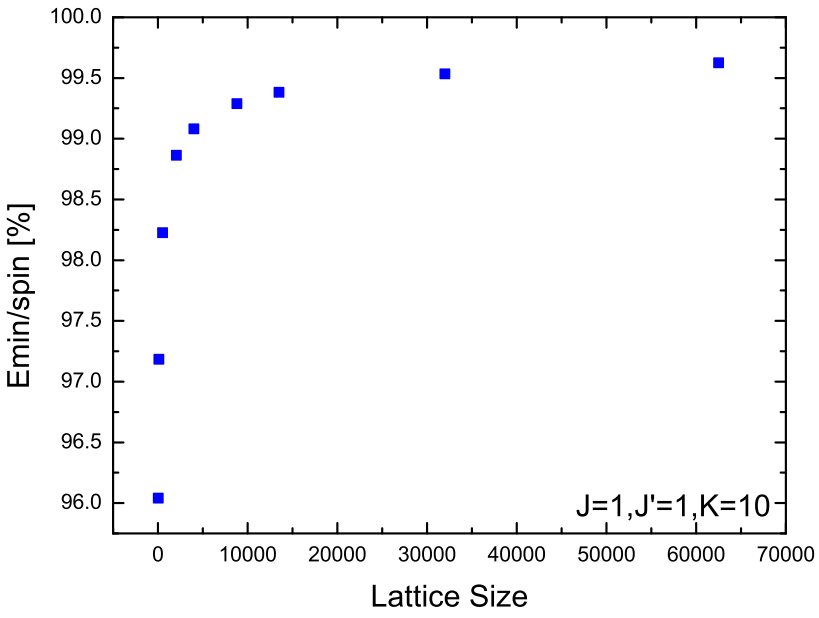

Figure 3.3: A plot of the energy per spin, in percents, for a q=0 distorted lattice, as calculated by the simulation, versus lattice size. The asymptotic value for an infinite lattice is of course 100%.

3.3 Finite Size Effects

In order to estimate the simulation error we needed to see how the finite size of the simulation lattice affected the final output of the simulation; in other words, we had to determine how characteristic output values of the simulation, such as total lattice energy, depend on the lattice size, and whether these values converge to an asymptotical value that corresponds to an infinite lattice. To this end, we plotted the calculated energy per spin of the simulation lattice versus lattice size, for a lattice structure whose energy can be calculated analytically: the $q = 0$ distorted lattice which will be discussed in section (3.5.1). This plot is shown in fig.(3.3). The energy is given in percents of the expected energy of an infinite lattice.

From the plot it can be verified that the energy per spin converges to the analytical value for an infinite lattice. The difference between the asymptotic value of the energy per spin and the actual value obtained from the simulation served as a measure of the simulation error, and guided us in the choice of the

lattice size. Ideally, we would like to use a lattice as big as possible; however, lattice size is limited by the time it takes the computer to finish a simulation run. By repeating each simulation run several times, we eliminated other computer-precision errors and determined finite size effects to be the main cause for error in our simulation.

3.4 Simulation Validation-Cubic Lattice

Before using the simulation program to obtain data as the basis of new research it is necessary to ensure that the program works correctly. This is done by reproducing some known results. The classical antiferromagnetic ground state on a simple cubic lattice is well known; it consists of two sublattices of equal and opposite magnetizations. A simple cubic lattice is comparable to the pyrochlore lattice in the coordination number; each spin has 6 near-neighbours. The distance between near neigbours in the cubic lattice is unity, same as will be used for the pyrochlore lattice.

We therefore run the simulation on a cubic lattice of 1000 and 8000 spins, with and without the magnetoelastic term. Since in a cubic lattice there is no geometrical frustration, we do not expect to obtain any distortion in a cubic lattice with the Hamiltonian (3.8).

We show in fig. (3.4) the neutron scattering and magnetic neutron scattering from a cubic lattice with 8000 antiferromagnetic spins, superimposed. On the left hand side of the figure we present the final state obtained by the simulation when minimizing the AF Heisenberg Hamiltonian, whereas on the right hand side we show the final state obtained by the simulation when minimizing the Hamiltonian (3.8) on a simple cubic lattice.

The scattering vector is in the [111] direction. The distance between planes in this direction is $d = 0.5774$, which results in scattering peaks at $|\mathbf{q}| \sim 10.9$. The AF correlation between spins creates two magnetic sublattices with twice the unit cell, thus resulting in magnetic scattering peaks at $|\mathbf{q}| \sim 5.4$, corresponding to twice the interplanar distance $d = 1.55$.

The neutron scattering shows no significant difference in the lattice structure and spin orientation between the minimization of the Heisenberg Hamiltonian and the minimization of the Hamiltonian (3.8), as expected. Moreover, we obtain the AF spin arrangement we anticipated.

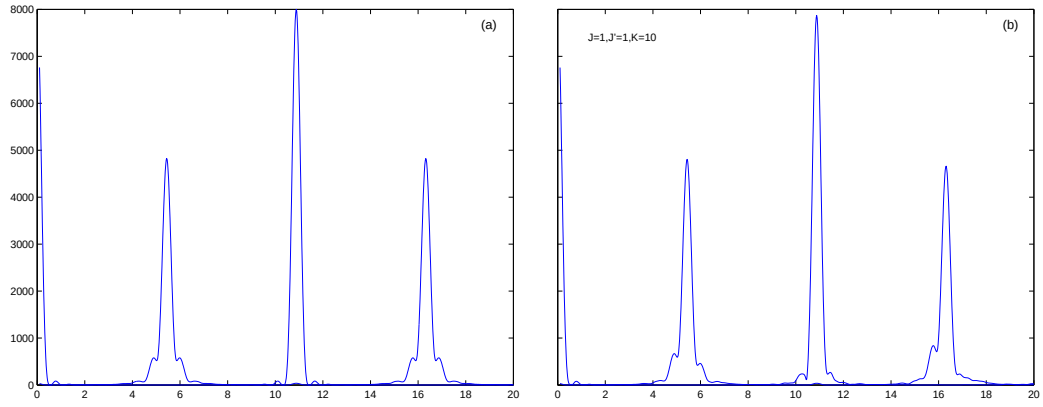

Figure 3.4: Neutron scattering from a cubic lattice of 8000 spins, obtained from minimizing (a) the AF Heisenberg Hamiltonian and (b) the magnetoelastic Hamiltonian.

3.5 The Initial Simulation State

It is natural to expect that the final state reached by the simulation will depend on the state it begins from. We know that the Heisenberg Hamiltonian with antiferromagnetic exchange couplings on the pyrochlore lattice gives us a ground state manifold which is completely ergodic; Moessner and Chalker [1] show, that it is possible to deform any ground state into any other ground state without any cost in energy. However, we do not know how the magnetoelastic terms change the ground state manifold, and whether it maintains its ergodicity. Therefore, trying different initial states in the simulation can give us some feeling as to the energy landscape in the presence of the magnetoelastic terms in the Hamiltonian. We ran the simulation while starting from several different initial states; we will present here the results obtained when starting from an initial state with random spin orientations, and from the $q = 0$ initial state.

3.5.1 The $q = 0$ Initial State

We chose a the $q = 0$ distortion presented in (1.1.1) as one of the initial states for the simulation. Eq. (1.31) gives us the shift from the initial location of the atoms in a tetrahedron. This has to be implemented on our simulation lattice. However, we need to remember that the axes used by the simulation are rotated relative to the axes in which it was natural to calculate the distortion; therefore, we rotate the new coordinates (after applying the distortion) using the matrix R^T (the matrix R given in (3.1)

describes the rotation of the axes and not of the coordinates).

The new distorted coordinates:

1. $(0,0,0)$
2. $(\sqrt{2}/2+\frac{-J'}{\sqrt{2}k},\sqrt{2}/2+\frac{-J'}{\sqrt{2}k},0)$
3. $(0,\sqrt{2}/2+\frac{-J'}{\sqrt{2}k},\sqrt{2}/2+\frac{3J'}{\sqrt{2}k})$
4. $(\sqrt{2}/2+\frac{-J'}{\sqrt{2}k},0,\sqrt{2}/2+\frac{3J'}{\sqrt{2}k})$

After rotating we obtain:

1. $(0,0,0)$
2. $(1-\frac{J'}{k},0,0)$
3. $(1/2-\frac{J'}{2k},\sqrt{3}/2+\frac{5\sqrt{3}J'}{6k},\frac{2\sqrt{2}J'}{\sqrt{3}k})$
4. $(1/2-\frac{J'}{2k},\sqrt{3}/6+\frac{7\sqrt{3}J'}{6k},\sqrt{2/3}+\frac{\sqrt{2/3}J'}{k})$

This is the basis we used to build the simulation lattice, instead of the undistorted basis:

1. $(0,0,0)$
2. $(1,0,0)$
3. $(1/2,\sqrt{3}/2,0)$
4. $(1/2,\sqrt{3}/6,\sqrt{2/3})$

so that the new matrix B_d that replaces (3.3) is given by:

$$B_d=\begin{pmatrix}1-\frac{J'}{k} & 1/2-\frac{J'}{2k} & 1/2-\frac{J'}{2k}\\ 0 & \sqrt{3}/2+\frac{5\sqrt{3}J'}{6k} & \sqrt{3}/6+\frac{7\sqrt{3}J'}{6k}\\ 0 & \frac{2\sqrt{2}J'}{\sqrt{3}k} & \sqrt{2/3}+\frac{\sqrt{2/3}J'}{k}\end{pmatrix} \tag{3.11}$$

When $J'/k\to 0$, it is easy to see that we obtain the undistorted lattice again.

Again, in order to verify the structure of the new lattice, and compare it to the undistorted structure, we performed neutron scattering, adjusting the scattering vector to the new [111] direction (this is tantamount to making sure our crystal is glued to the sampleholder in a real experiment) . This is

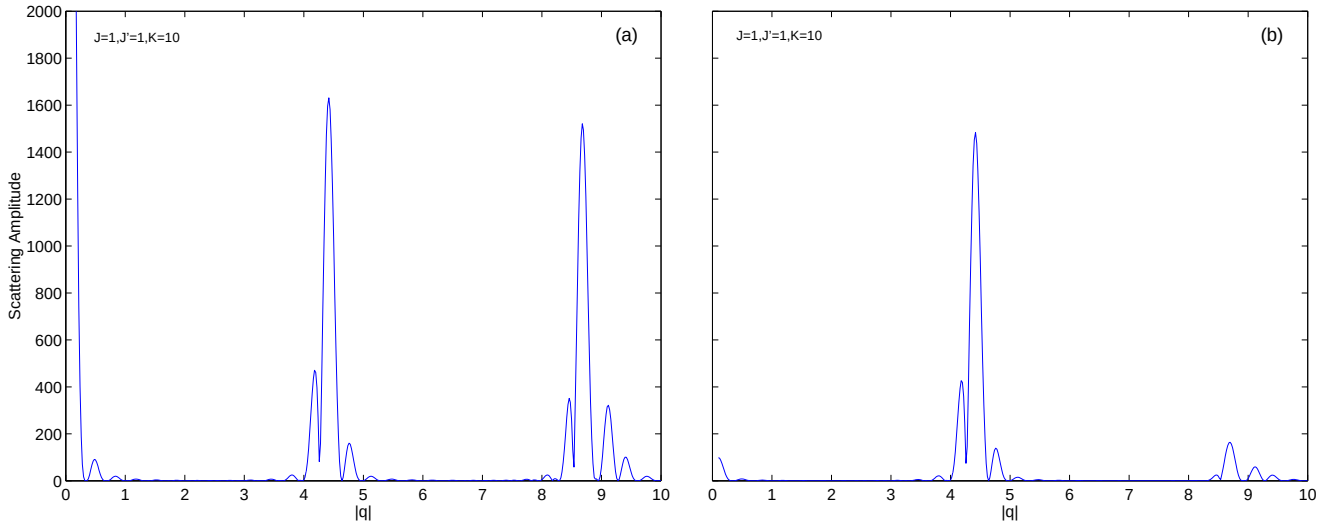

Figure 3.5: Neutron scattering from a pyrochlore lattice of 8788 spins, with the q=0 distortion. In (a) we see the spatial part and in (b) the magnetic part.

shown in fig. (3.5). Indeed, we see splittings in the scattering intensity peaks, which are caused by atoms moving to below and above the lattice planes, accompanied by a shift in the location of the peaks, which stems from a shortening of the distance between lattice planes, namely a shrinking of the entire lattice. When looking at the magnetic scattering, we see again that we obtain the peak that corresponds to only half of the structural planes (kagomé-kagomé and triangular-triangular), due to the different magnetic periodicity.

It is also useful to look at the spin orientations and the near-neighbour spin-spin correlation distribution, for comparison to the final states obtained by the simulation (fig. 3.6). In this state all spins are oriented either parallel or antiparallel to the z-axis, such that 2/3 of the bonds are antiferromagnetically correlated and thus satisfied, and 1/3 of the bonds are ferromagnetically correlated and frustrated.

3.5.2 Random initial state

This is a state in which the directions of the spins were chosen at random using a randomization algorithm, while the spin locations remain unchanged from the initial ordered pyrochlore lattice locations.

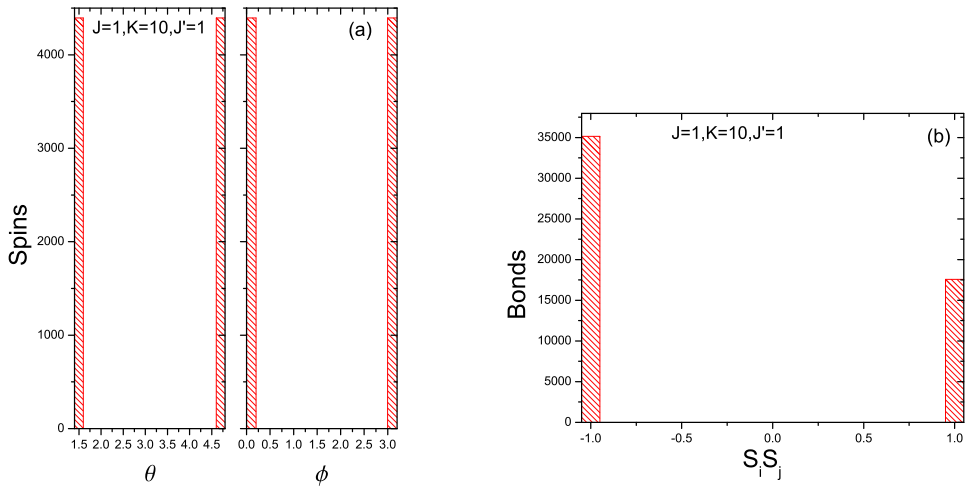

Figure 3.6: (a) Distribution of spin orientations in the q=0 state. θ and ϕ are, respectively, the azimuthal and polar angles. (b) Distribution of near-neighbour spin-spin correlations in the q=0 initial state. 2/3 of the bonds are completely satisfied with $S_iS_j = -1$, and 1/3 of the bonds are completely frustrated with $S_iS_j = 1$.

3.6 Simulation Results

We plotted the total energy of the lattice, calculated after the simulation run, as a function of the parameter J'^2, with k kept fixed. We expect the relation (3.9) to hold in the linear distortion limit, where $J'/k \to 0$. The error in the final energy value obtained was determined as described in section (3.3).

From fig. (3.7) we see that the minimal energy obtained depends on the initial state chosen; however, for small J'^2 the differences are not significant. For $J'^2 < 1$ when starting from the $q = 0$ state, the energy calculated at the end of the simulation matches the theoretical value, whereas the random spin-arrangement initial state results in a final state which is higher in energy. The energies of the final states exhibit a divergence from linearity with increasing J'^2 (which actually means increasing J'^2/k, since k is kept fixed).

The difference between the theoretical energy value, calculated from the expression (1.9), and the final energy value obtained by the simulation, stems almost entirely from the fact that the simulation calculates the actual δr for each bond and not only the first-order change. This can be seen by calculating numerically the energy of the $q = 0$ state after it is input to the simulation (the green line in fig. (3.7)), and comparing it to its theoretical

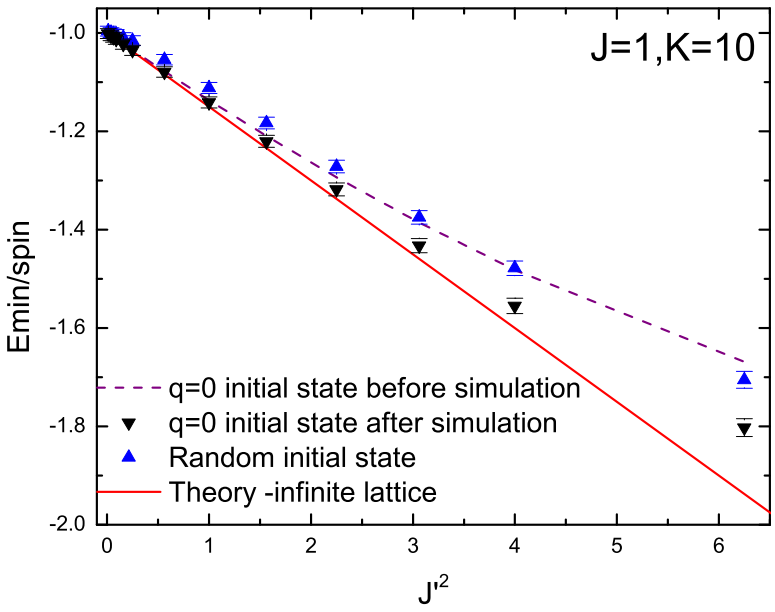

Figure 3.7: The minimum energy per spin obtained from the simulation, for the q=0 and random spins initial states, versus J'^2. We also show here the energy of the initial q=0 state and the theoretical value of the energy (3.10).

value for different J's. The ratio $E_{q=0}/E_{theory}$ (fig. 3.8) goes to 1 in the limit $J'^2/k \to 0$, and decreases with increasing J'^2/k.

The final lattice structures obtained from the simulation are also different from theoretical ground state $q = 0$. Whereas the final state obtained from the $q = 0$ state retained the initial spin ordering, the structure of the distortion changed.

When starting from a nondistorted initial state with random spin orientations, we obtained a distorted final state, with short-range spin order. This can be seen in the spin-spin correlations as extracted from the post simulation data (Fig. (3.9 (b)). Moreover, from the distribution of the spins orientations in the final state obtained from the simulation (Fig. (3.9 (a)), we can see that the spins are arranged in the $x - y$ plane, but with orientations uniformly distributed within that plane.

Looking back at (3.6), we note that the new state obtained from a nondistorted initial state is similar locally to the $q = 0$ state; 2/3 of the bonds are antiferromagnetically correlated and thus satisfied, and 1/3 of the bonds are

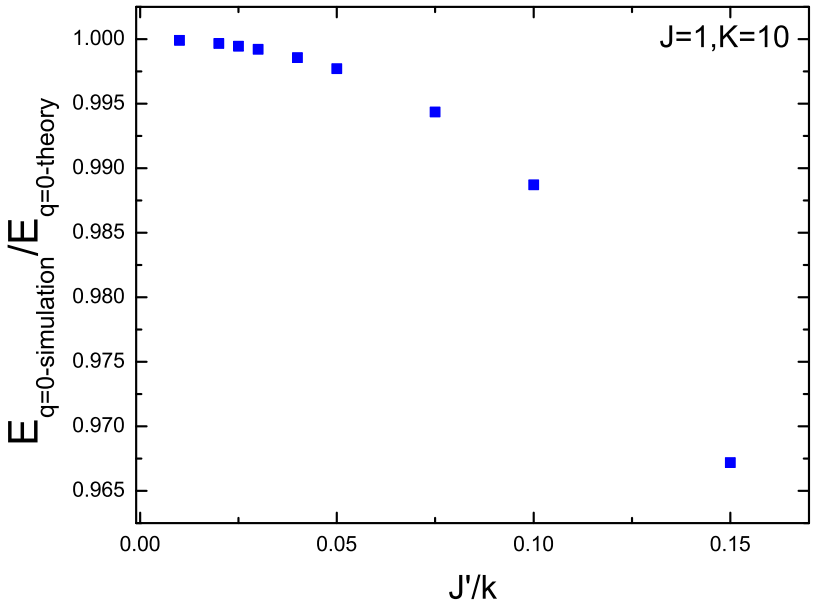

Figure 3.8: The ratio $E_{q=0}/E_{theory}$ vs. J'/k for a lattice size of 8788 spins.

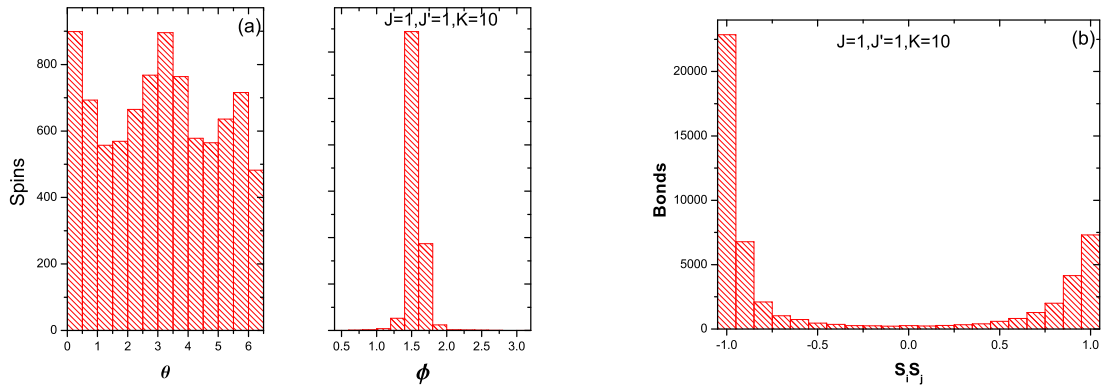

Figure 3.9: (a)The spin orientation distribution for the final simulation state obtained from a random spin arrangement initial state. (b)Distribution of near-neighbour spin-spin correlations in the final simulation state obtained from a random spin arrangement initial state.

ferromagnetically correlated and frustrated.

In Fig.(3.10) we show the neutron scatterings from all the final structures obtained with the simulation. These scatterings have several signatures- first of all, we see a shrinking of the lattice in the shift of the scattering peaks to the right, for instance from $|\mathbf{q}| \sim 3.85$ to $|\mathbf{q}| \sim 4.4$ for the $q = 0$ final state and $|\mathbf{q}| \sim 4$ for the final state obtained from a random spins initial state. Secondly, we see splittings in the scattering peaks, which mean that atoms have moved in and out of the kagomé and triangular planes.

Whereas in the final state obtained from a random initial state we see no long range magnetic correlations, in the initial and final q=0 states we see long range magnetic order. On the right side of the figure we see the magnetic scatterings, and on the left side we see the nonmagnetic scatterings. Whereas the q=0 initial state maintains the initial magnetic arrangement,the final state obtained from an undistorted random-spins initial state shows no correlation between the magnetic and spacial arrangement, and hence no signal in the magnetic neutron scattering. In order to ensure that this lack of signal is not due to the specific choice of the scattering vector, we tried scattering vectors with several different orientations and still, obtained no signal.

We see here that the final state obtained from the simulation is strongly dependent upon the initial conditions. Whereas locally, the final states are similar, one state (the one obtained from the q=0 state) exhibits long range magnetic order, whereas the other does not. The difference in energy between the ordered and disordered final states is approximately linear in J'^2, starting from less than 1% of the final energy value for small J'^2, and increasing to several percents.

To conclude this section, our main discovery was that the $q = 0$ state is the lowest energy state for the Hamiltonian, yet when the simulation starts from a random initial spin arrangement, it reaches a final state which is very different from the $q = 0$ state.

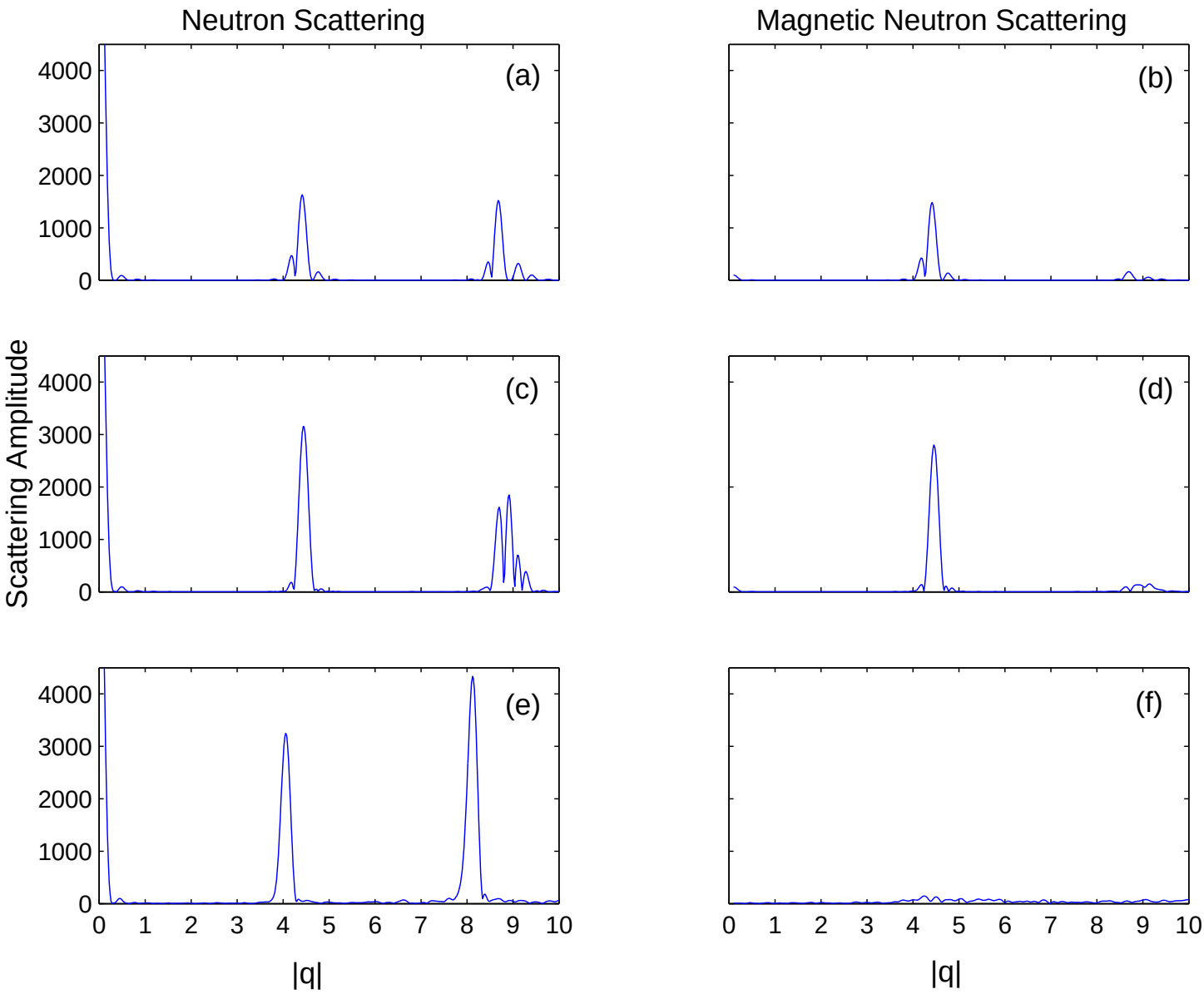

Figure 3.10: Virtual neutron scattering from the lattice structures obtained from the simulation, for J=1, J'=1, K=10. (a)-(b) show the scattering from the initial q=0 state, (c)-(d) show the scattering from the final state obtained by the simulation when starting from the initial q=0 state, and (e)-(f) show the scattering from the state obtained from an initial random-spins arrangement.

3.7 Increasing the Temperature

The findings of the previous section led us to enquire as to the nature of low excited states of the pyrochlore system; namely, what happens to the $q = 0$ state when we raise the temperature from $T = 0$? We implemented such a temperature increase in the simulation through a reverse simulated-annealing algorithm. We included a Boltzmann factor $F_B = \exp \Delta E/T$, that enables the system to 'jump' into states which are not energetically favourable, with probability $p < \exp \Delta E/T$, and slowly increased the temperature from $T = 0$ to various final values. The parameter δE is the energy difference (for one spin) between two different location and orientation values. To validate this part of the simulation, we verified that for $F_B = 0$ the system goes to the final state obtained from the initial $q = 0$ state, without temperature.

As the temperature per spin is increased, the crystal slowly melts and loses its structure and spin ordering. This is because of the open boundary conditions, which were required to enable a non volume preserving distortion of the crystal (such as the $q = 0$ state). However, there is information to be gained from this melting process. We performed virtual neutron scattering on the states obtained, at temperatures of $T = 0.1J - T = 0.000001J$ per spin. We show three temperatures -$0.0001J - 0.000001J$ in fig. (3.11). We notice that the splittings in the second peak (the kagomé-kagomé triangular-triangular peak), which are evidence of the lattice distortion, disperse and are no longer evident at a temperature of only $0.0001J$ per spin. In contrast, the magnetic scattering peak at $|\mathbf{q}| \sim 4.4$, which manifests the magnetic ordering in the lattice, persists at this temperature.

In fig. (3.12 (e)-(f)) we show the scattering at $T = 0.001J$ with two reference scatterings- from the initial $q = 0$ state (3.12 (c)-(d)) and from a pyrochlore lattice with spins that satisfy the requirement that the sum of spins on each tetrahedron be zero (3.12 (a)-(b)). We see here clearly that the splittings which characterize the $q = 0$ state are no longer visible at this temperature, whereas the magnetic scattering peak can still be discerned. As T increases, lattice distortions are not observable, but spin correlations still are.

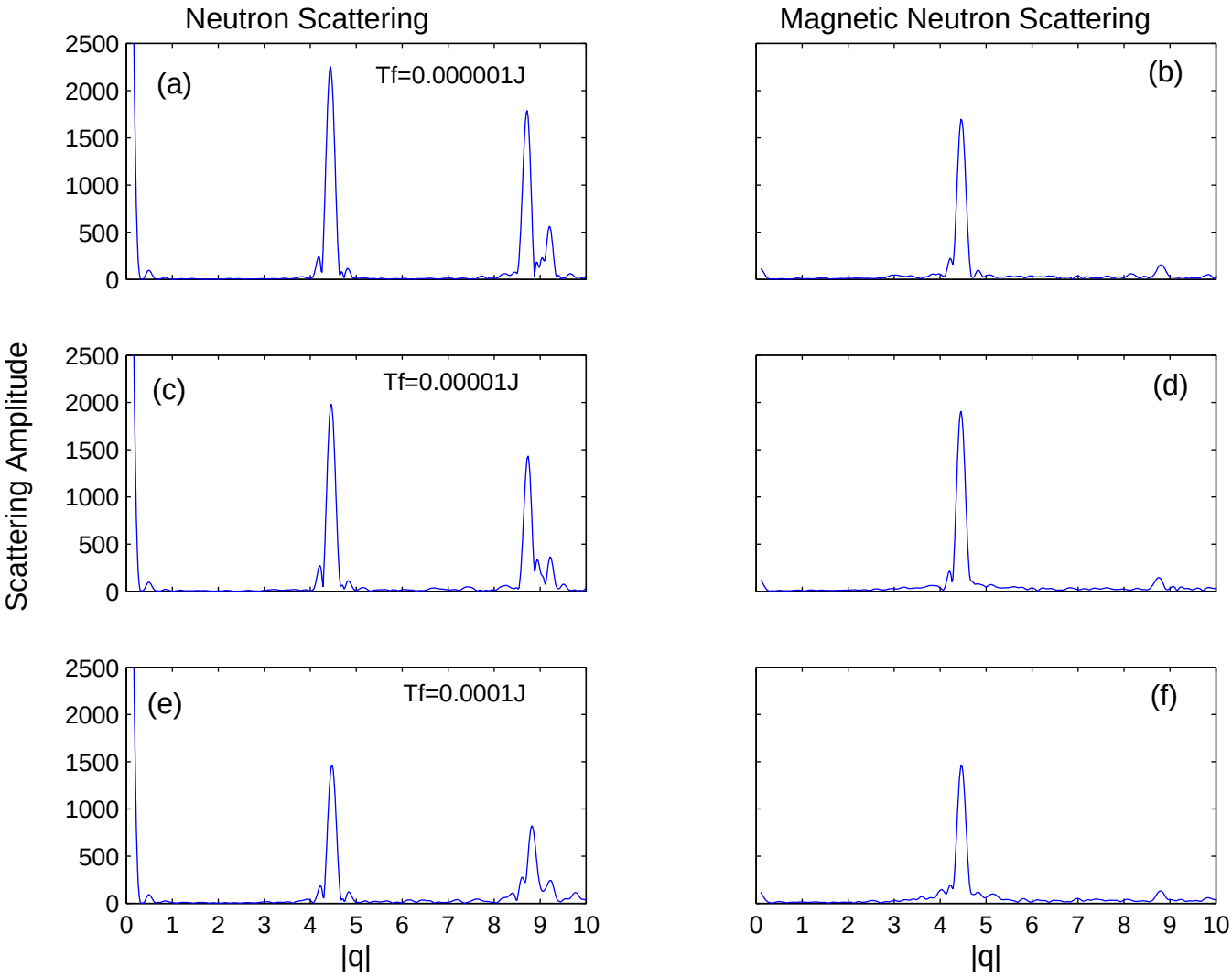

Figure 3.11: Neutron scattering and magnetic neutron scattering from the final states obtained from the initial q=0 state for J=1, J'=1, K=10, upon increasing the temperature. Three temperatures are shown.

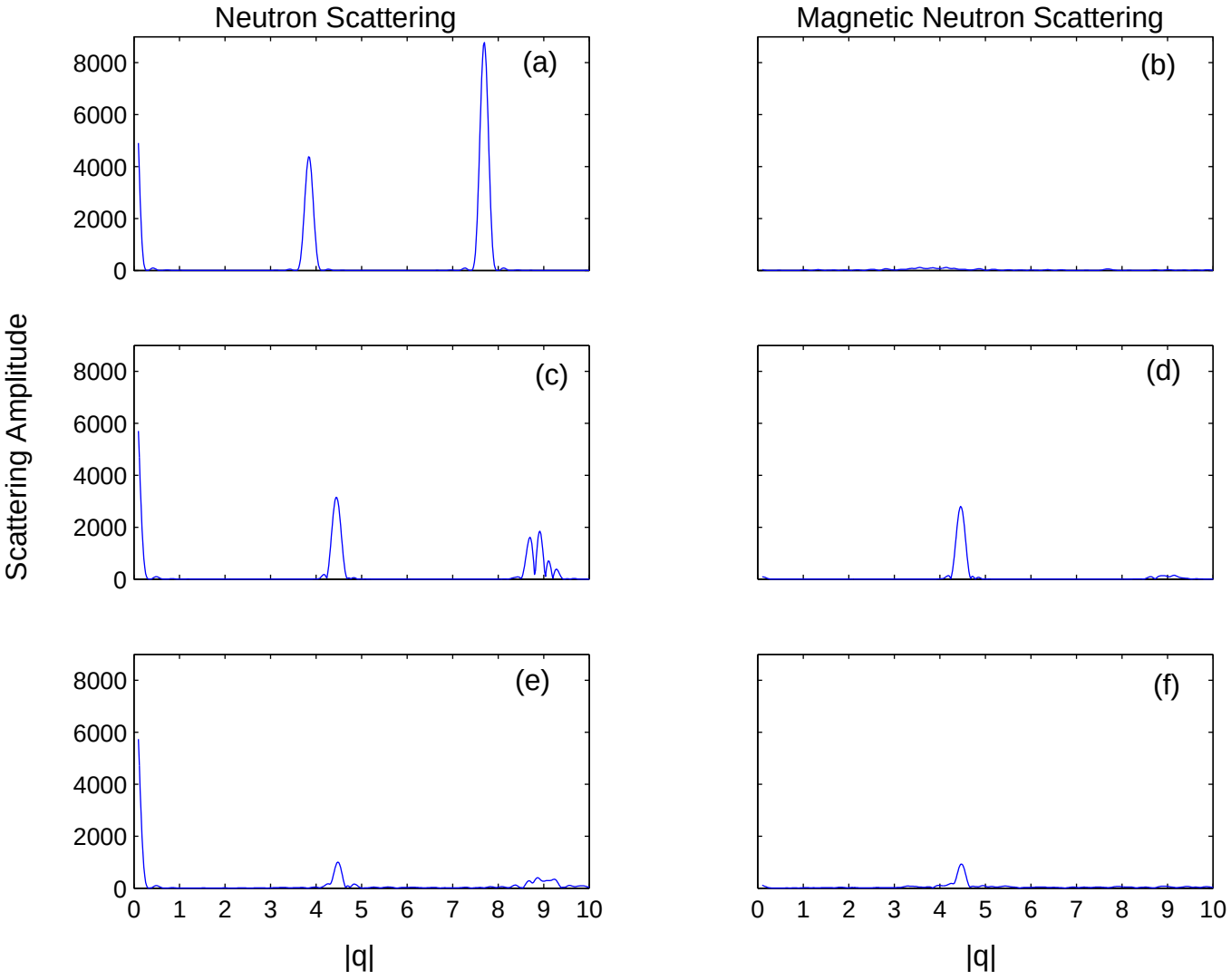

Figure 3.12: (a)-(b) show neutron and magnetic neutron scattering from an ordered pyrochlore lattice in one of the degenerate ground states of the Heisenberg Hamiltonian. (c)-(d)show neutron and magnetic neutron scattering from the $q = 0$ initial state. (e)-(f) show neutron and magnetic neutron scattering from the state obtained from the $q = 0$ initial state when temperature is increased to $0.001J$. All data are for J=1, J'=1, K=10.

Chapter 4

Conclusions

In this work we investigated the ground state of the pyrochlore lattice with AF Heisenberg Hamiltonian, in the presence of a magnetoelastic term which enables the lattice to distort and decrease the magnetic energy. We performed μSR and magnetization measurements on the pyrochlore $Y_2Mo_2O_7$, for which there was previous evidence of lattice distortion [17], and complemented the experiments with computer simulations that modelled an ideal pyrochlore lattice.The simulation data was analyzed by means of a Matlab script that performed both magnetic and non-magnetic neutron scattering.

The μSR and magnetization data pointed at a change in the local magnetic environment within the compound, as the temperature is lowered. However, we were unable to characterize the exact nature of this change; it is likely that it stems from a disordered lattice distortion which causes a distribution of different fields at the muon site, in contrast to the theoretical prediction. To address this discrepancy we performed numerical simulations.

Our simulations looked for the minimum energy state at T=0 of a pyrochlore lattice, using the Heisenberg Hamiltonian with a magnetoelastic term (3.8), and explored the nature of excited states when starting from a particular theoretical ground state. The non-temperature dependent part of the simulation was set to run from two different initial states:

1. Lattice structure is distorted to a state obtained from minimizing a linearized Hamiltonian (1.9), and spins arranged in a corresponding antiferromagnetic orientation. We termed this state the $q = 0$ state.

2. Pyrochlore lattice structure, with random spin orientation.

We discovered that initial states 1 and 2 resulted in essentially dissimilar final states, with different energy values and spin ordering. The value of the total lattice energy attained was higher when starting from state (2), and

both values of the total lattice energy were higher than the theoretical value given by (3.10). However, the simulation and the theoretical energies agree in the $J'/k \Rightarrow 0$ limit. Whereas the final state obtained from state (1) was characterized by long-range spin order, in the final simulation state obtained from state (2) we witnessed no spin correlations and a randomly distributed distortion accompanied by a shrinking of the entire lattice.

When temperature was increased from the $q = 0$ initial state, the characteristic signatures of the $q = 0$ state that were visible in the virtual neutron scattering, namely a multiply split scattering peak and a magnetic scattering peak, started to disperse. However, the splitting in the neutron scattering disappeared at a temperature lower than that at which the magnetic scattering peak was no longer evident.

The combined experimental and simulation data led us to conclude:

- The structure of the minimum energy state obtained from the simulation is different from the structure of the minimum energy state predicted by theory, due to nonlinear distortion terms which the simulation takes into account but the theory doesn't. It turns out, that the nonlinear distortion terms result in an increase of the lattice energy.

- The spin-ordered lattice-distorted minimum energy configuration we discovered is very close in energy to other distorted states with no apparent magnetic order, as can be seen both from the simulation runs which start from undistorted initial states, and from the temperature increases performed on the q=0 state.

- The fact that the final state attained by the simulation depended so strongly on the initial state, hints at a non-ergodic ground state manifold for the Hamiltonian (3.8). It could well be that a magnetoelastic term in the Hamiltonian would lead to both a disordered and ordered distortion, depending on other parameters which were not tested in this work.

- As temperature is increased, the spatial characteristics of the ordered $q = 0$ ground state disperse, whereas the magnetic correlations persist at a temperature of $T = 0.001J$. This means that if some magnetically ordered distorted state sets in at low temperatures in our compound, it is more likely to be discovered by magnetic probes such as μSR and NMR than by probes that look for the spatial features of the distortion. As a result of the non-zero temperature which leads to non-long range magnetic order, the magnetic probes will experience a random field distribution. Thus our simulation provides an insight has to why we

detect only broadening of the μSR line rather than a set of distinct frequencies.

4.1 Future Plans

The work presented in this thesis can be continued along two parallel complementary lines- the computational and the experimental.

From the computational point of view, the fact that the final energy obtained by the simulation when starting from a random initial state, was higher than the theoretical predicted value, indicates the need for a different strategy in seeking the minimum energy state of the Heisenberg and magnetoelastic Hamiltonian on the pyrochlore lattice. In this work we implemented a Monte Carlo algorithm at $T = 0$, hoping that it would suffice to find the sought-after ground state, since it succeeded in finding the ground states for the Heisenberg Hamiltonian on the pyrochlore lattice. However, the strong dependence of the final state obtained by the simulation on the initial state suggests, that the Monte Carlo algorithm is not enough and that a simulated annealing approach is required. The concept of simulated annealing is based on the manner in which liquids freeze or metals recrystalize in the process of annealing. In an annealing process a melt, initially at high temperature and disordered, is slowly cooled so that the system at any time is approximately in thermodynamic equilibrium. As cooling proceeds, the system becomes more ordered and approaches a "frozen" ground state at T=0. Hence the process can be thought of as an adiabatic approach to the lowest energy state. If the initial temperature of the system is too low or cooling is done insufficiently slowly the system may become quenched forming defects or freezing out in metastable states (ie. trapped in a local minimum energy state). However, if the process is carried out correctly, the system avoids being trapped in local minima and attains the global minimum.

However, implementation of a simulated annealing algorithm holds in store several substantial difficulties. The algorithm employs a random search which not only accepts changes that decrease the function to be minimized,E, but also some changes that increase it. The latter are accepted with a probability $p = \exp \Delta E/T$, where ΔE is the increase in E and T is the system temperature. Thus there are several user-defined parameters which have to be determined correctly:

- The initial temperature of the system T_0.
- The final temperature of the system T_f.

- The cooling rate - the rule according to which the temperature is decremented.

The correct choice of these parameters is by no means trivial and requires a large amount of calibration. We tried to implement a simulated annealing algorithm on our system, however we failed to obtain meaningful results in the time frame available. The natural and necessary continuation of our work would be to successfully implement a simulated annealing algorithm for the pyrochlore lattice, which would resolve the questions that remain open regarding the nature of the minima obtained by the simulation.

From the experimental point of view, a more thorough investigation of the structure of $Y_2Mo_2O_7$ in various magnetic fields and temperatures would be interesting. This could include measuring the μSR relaxation from static fields only, what we termed Δ in Chapter 2, versus the magnetic field applied, at constant temperature. Another possible experimental avenue would be to perform neutron scattering in an external magnetic field. Such an experiment was not carried out yet, and it would serve to determine whether there is some correlation between the lattice distortion observed by magnetic probes and the magnetic fields applied to carry out those measurements.

Appendix A

Neutron Scattering

Here we will show how we obtain the differential cross-section, and hence the scattering amplitude, for elastic neutron scattering.

Suppose we have a neutron of wavevector $\mathbf{k}$ incident on a scattering system characterized by an index λ. Let the neutron be in a state Ψ_k and the scattering system in a state χ_λ.We assume an interaction potential V between the neutron and the system, which scatters the neutron into a state with wavevector $\mathbf{k}'$, and leaves the system in a final state λ'. Denote the number of nuclei in the scattering system by N, the position vectors of these nuclei by $\mathbf{R}_j$, and the position of the neutron by $\mathbf{r}$.

The differential cross section is given by:

$$\left(\frac{d\sigma}{d\Omega}\right)_{\lambda\to\lambda'} = \frac{1}{\Phi}\frac{1}{d\Omega}\sum_{\mathbf{k}'\in d\Omega} W_{\mathbf{k},\lambda\to\mathbf{k}',\lambda'} \tag{A.1}$$

where $W_{\mathbf{k},\lambda\to\mathbf{k}',\lambda'}$ is the number of transitions per second between the states $\mathbf{k},\lambda$ and $\mathbf{k}',\lambda'$ and Φ is the flux of incident neutrons.

By Fermi's Golden Rule:

$$\sum_{\mathbf{k}'\in d\Omega} W_{\mathbf{k},\lambda\to\mathbf{k}',\lambda'} = \frac{\mathcal{V}}{(2\pi)^2\hbar^3} m\mathbf{k}' | < \mathbf{k},\lambda|V|\mathbf{k}',\lambda' > |^2 \tag{A.2}$$

assuming box normalization.

The transition matrix element is given explicitly by:

$$< \mathbf{k},\lambda|V|\mathbf{k}',\lambda' >= \int_{\mathcal{V}} \Psi^*_{k'}\chi^*_{\lambda'} V \Psi_k \chi_\lambda d\mathbf{R} d\mathbf{r} \tag{A.3}$$

Substitute for the neutron wavefunction:

$$\Psi_{\mathbf{k}} = \frac{1}{\sqrt{\mathcal{V}}}\exp\left(i\mathbf{k}\cdot\mathbf{r}\right) \tag{A.4}$$

$$< \mathbf{k}, \lambda | V | \mathbf{k}', \lambda' >= \frac{1}{\mathcal{V}} \int_{\mathcal{V}} \exp\left(-i\mathbf{k}' \cdot \mathbf{r}\right) \chi^*_{\lambda'} V \exp\left(i\mathbf{k} \cdot \mathbf{r}\right) \chi_\lambda d\mathbf{R} d\mathbf{r} \tag{A.5}$$

We need to substitute a specific function for the interaction potential V. Since we are only interested in the spatial structure of the lattice, we can make V really short range, and put: $V(\mathbf{R}) = \delta(\mathbf{R})$. Hence the potential for the whole scattering system is:

$$V = \sum_j \delta(\mathbf{r} - \mathbf{R}_j) \tag{A.6}$$

It is convenient to define a new variable in order to complete the integration over $\mathbf{r}$: $\mathbf{x}_j = \mathbf{r} - \mathbf{R}_j$. The transition matrix element becomes:

$$< \mathbf{k}, \lambda | V | \mathbf{k}', \lambda' > \propto \sum_j \int \exp\left(-i\mathbf{k}' \cdot (\mathbf{x}_j + \mathbf{R}_j)\right) \chi^*_{\lambda'} \delta(\mathbf{x}_j) \exp\left(i\mathbf{k} \cdot (\mathbf{x}_j + \mathbf{R}_j)\right) \chi_\lambda d\mathbf{R} d\mathbf{x}_j =$$

$$= \sum_j \int \delta(\mathbf{x}_j) \exp\left(i\left(\mathbf{k} - \mathbf{k}'\right) \cdot \mathbf{x}_j\right) d\mathbf{x}_j \chi^*_{\lambda'} \exp\left(i\left(\mathbf{k} - \mathbf{k}'\right) \cdot \mathbf{R}_j\right) \chi_\lambda d\mathbf{R} \tag{A.7}$$

Define the scattering vector κ:

$$\mathbf{q} = \mathbf{k} - \mathbf{k}' \tag{A.8}$$

Since $\int \delta(\mathbf{x}_j) \exp\left(i\mathbf{q} \cdot \mathbf{x}_j\right) d\mathbf{x}_j = 1$, we are left with:

$$< \mathbf{k}, \lambda | V | \mathbf{k}', \lambda' > \propto \sum_j \int \chi^*_{\lambda'} \exp\left(i\kappa \cdot \mathbf{R}_j\right) \chi_\lambda d\mathbf{R} =$$

$$= < \lambda | \sum_j \exp\left(i\mathbf{q} \cdot \mathbf{R}_j\right) | \lambda' > \tag{A.9}$$

Remember that the scattering amplitude is proportional to the squared transition matrix element :

$$| < \mathbf{k}, \lambda | V | \mathbf{k}', \lambda' > |^2 \propto | < \lambda | \sum_j \exp\left(i\mathbf{q} \cdot \mathbf{R}_j\right) | \lambda' > |^2 \tag{A.10}$$

To obtain the differential cross section we need to sum over final states λ' and average over initial states λ:

$$\left(\frac{d\sigma}{d\Omega}\right) = \sum_{\lambda, \lambda'} p_\lambda \left(\frac{d\sigma}{d\Omega}\right)_{\lambda \to \lambda'} \tag{A.11}$$

First we note that the states λ' satisfy the closure relation:

$$\sum_{\lambda'} | < \lambda | \sum_j \exp\left(i\mathbf{q}\cdot\mathbf{R}_j\right) | \lambda' > |^2 =$$

$$= \sum_{\lambda'} < \lambda | \sum_{j'} \exp\left(-i\mathbf{q}\cdot\mathbf{R}_{j'}\right) | \lambda' > < \lambda' | \sum_j \exp\left(i\mathbf{q}\cdot\mathbf{R}_j\right) | \lambda > =$$

$$= < \lambda | \left| \sum_j \exp\left(i\mathbf{q}\cdot\mathbf{R}_j\right) \right|^2 | \lambda > \tag{A.12}$$

Now, $\sum_\lambda p_\lambda < \lambda | \left| \sum_j \exp\left(i\mathbf{q}\cdot\mathbf{R}_j\right) \right|^2 | \lambda >$ is actually the thermal average of the lattice sum $\left| \sum_j \exp\left(i\mathbf{q}\cdot\mathbf{R}_j\right) \right|^2$.

Hence the neutron scattering amplitude off our virtual lattice will be proportional to:

$$A \propto \left| \sum_j \exp\left(i\mathbf{q}\cdot\mathbf{R}_j\right) \right|^2 \tag{A.13}$$

Appendix B

Magnetic Neutron Scattering

The magnetic field at point R due to the electron spin:

$$B \propto \nabla \times (\frac{S \times R}{R^3}) \tag{B.1}$$

where R is the distance from the spin. This can be written as:

$$\nabla \times (\frac{S \times R}{R^3}) = \frac{1}{2\pi^2} \int \hat{q} \times (S \times \hat{q}) \exp(iq \cdot R) dq \tag{B.2}$$

since

$$\frac{R}{R^3} = -\nabla(\frac{1}{R}) \tag{B.3}$$

and ∇ operates only on R:

$$\nabla \times (\frac{S \times R}{R^3}) = -\nabla \times (S \times \nabla(\frac{1}{R})) \tag{B.4}$$

We also note that:

$$\int \frac{1}{R} \exp(-iq \cdot R) dr = \int_0^{2\pi} d\phi \int_{-1}^{1} dcos\theta \int_0^{\infty} R \exp(-iqRcos\theta) dR = 4\pi \int_0^{\infty} \frac{sinqR}{q} dR = \frac{2\pi}{q^2} \tag{B.5}$$

Therefore:

$$\nabla \times (S \times \nabla(\frac{1}{R})) = \int dq \frac{q \times (S \times q)}{q^2} \exp(-iq \cdot R) = \int \hat{q} \times (S \times \hat{q}) \exp(iq \cdot R) dq \tag{B.6}$$

The interaction between the neutron and the magnetic field generated by the electrons is proportional to $I \cdot B$ where I is the spin of the neutron.

The spatial part of the transition matrix element:

$$< k' \mid V_{S_i} \mid k > \propto \int \exp(-ik'r) \nabla \times (\frac{S_i \times R}{R^3}) \exp(ikr) dr \tag{B.7}$$

Where $r = r_i + R$. We switch to integration on R, since r_i, the location of the ion, is constant, and take $\kappa = k - k'$:

$$\int \exp(-ik'r)\nabla\times(\frac{S_i \times R}{R^3})\exp(ikr)dr = \frac{1}{2\pi^2}\int\int \exp(i\kappa(r_i+R))\hat{q}\times(S_i\times\hat{q})\exp(iq\cdot R)dqdR \tag{B.8}$$

The dR integration yields a factor of $\delta(\kappa+q)$, enabling us to perform the dq integration as well and write:

$$< k' \mid V_{S_i} \mid k >= 4\pi\exp(i\kappa r_i)(\hat{\kappa}\times(S_i\times\hat{\kappa})) \tag{B.9}$$

We can now define operators:

$$Q_\perp = \sum_i \exp(iq\cdot r_i)(\hat{q}\times S_i\times\hat{q}) \tag{B.10}$$

$$Q = \sum_i \exp(iq\cdot r_i)S_i \tag{B.11}$$

Such that:

$$Q_\perp = Q - (Q\cdot\hat{q})\hat{q} \tag{B.12}$$

Therefore, $Q_\perp$ is the projection of Q in the direction perpendicular to $\hat{q}$. Since the spins density is given by

$$\rho_s(r) = \sum_i \delta(r-r_i)S_i \tag{B.13}$$

then it is easy to see that Q is the fourier transform of the spins density.

Including the spin of the neutron we get the interaction between the neutron and the scattering system:

$$I\cdot\sum_i \exp(i\kappa r_i)(\hat{\kappa}\times(S_i\times\hat{\kappa})) \tag{B.14}$$

We need to calculate the squared matrix element of this operator between the initial and final spin states of the combined crystal and neutron system. Since the electron spin and neutron spin operate in orthogonal spaces, we can separate the matrix elements:

$$< i,s \mid I\cdot Q_\perp \mid i's' >=< i \mid I \mid i' >< s \mid Q_\perp \mid s' > \tag{B.15}$$

squaring, we get:

$$|< i \mid I \mid i' >|^2 |< s \mid Q_\perp \mid s' >|^2 \tag{B.16}$$

This needs to be averaged over initial states and summed over final states:

$$\sum_{i,i',s,s'} p_i p_s | < i \mid I \mid i' > |^2 | < s \mid Q_\perp \mid s' > |^2 = \sum_{i,s} p_i p_s < i \mid II^\dagger \mid i >< s \mid Q_\perp Q_\perp^\dagger \mid s > \tag{B.17}$$

p_i and p_s are the probabilities for initial states i and s. It is useful to note that:

$$\begin{aligned} Q_\perp Q_\perp^\dagger &= (Q - (Q \cdot \hat{q})\hat{q})(Q - (Q \cdot \hat{q})\hat{q})^\dagger = QQ^\dagger - (Q \cdot \hat{q})(Q^\dagger \cdot \hat{q}) = \\ &= \sum_\alpha Q_\alpha Q_\alpha - \sum_{\alpha,\beta} (Q_\alpha q_\alpha)(Q_\beta q_\beta) = \sum_{\alpha,\beta} (\delta_{\alpha\beta} - q_\alpha q_\beta) Q_\alpha Q_\beta \end{aligned} \tag{B.18}$$

The average over neutron spin states gives a constant, and since we deal with **classical spins**, the scattering cross section is proportional to:

$$\begin{aligned} \sum_{\alpha,\beta} (\delta_{\alpha\beta} - q_\alpha q_\beta) Q_\alpha Q_\beta &= \sum_{\alpha,\beta} (\delta_{\alpha\beta} - q_\alpha q_\beta) \sum_{i,j} \exp(iq(r_i - r_j)) S_\alpha^i S_\beta^j = \\ &= \sum_{\alpha,\beta} (\delta_{\alpha\beta} - q_\alpha q_\beta) \sum_{i,j} S_\alpha^i S_\beta^j \cos(q(r_i - r_j)) \end{aligned} \tag{B.19}$$

Bibliography

[1] R. Moessner and J. T. Chalker, Phys. Rev. B 58, 12049 (1998)

[2] J. N. Reimers and A. J. Berlinsky, Phys. Rev. B 48, 9539 (1993)

[3] J. Villain , R. Bidaux, J. P. Carton and R. J. Conte, J. Phys. (Paris) 41,1263 (1980)

[4] K. Terao, J. Phys. Soc. Jpn. 65,1413 (1996)

[5] Y. Yamashita and K. Ueda, Phys. Rev. Lett. 85,4960 (2000)

[6] O. Tchernyshyov, R. Moessner, S.L.Sondhi, Phys. Rev. Lett. 88, 067203 (2002)

[7] O. Tchernyshyov, R. Moessner, S.L.Sondhi, Phys. Rev. B 66 (2002)

[8] Y. Ueda, N. Fujiwara, H. Yasuoka, J. Phys. Soc. Jpn. 66,778 (1997)

[9] H. Mamyia el al., J. Appl. Phys. 81, 5289 (1997)

[10] J.S.Gardner et al., PRL 83, 211 (1999)

[11] Ph.-H. Hubert, Bull. Chem. Soc. France 2385 (1974).

[12] M. A. Subramanian et al., Mater. Res. Bull. 15, 1401 (1980)

[13] N. P. Raju, E. Gmelin and R.K. Kremer, Phys. Rev. B. 46, 5405 (1992)

[14] S.R. Dunsiger et al., Phys. Rev. B 54, 5405 (1992)

[15] K. H. Fishcer and J. Hertz, Spin Glasses (Cambridge University, England, 1991)

[16] C.H Booth, J. S. Gardner, G. H Kwei, R. H. Heffner, F. Bridges and M. A. Subramanian, Phys. Rev. B 6, R755 (2000)

[17] Amit Keren and Jason. S. Gardner, Phys. Rev. Lett. 87, 177201 (2001)

[18] S. H. Lee et al. Phys. Rev. Lett. 84, 3718 (2000)

[19] M. P. Allen and D. J. Tildesley, Computer Simulation of Liquids (Oxford Science Publications, 1987)